Volume 24
Number 23
21 June 2022
Pages 14095–14664

PCCP

Physical Chemistry Chemical Physics

rsc.li/pccp

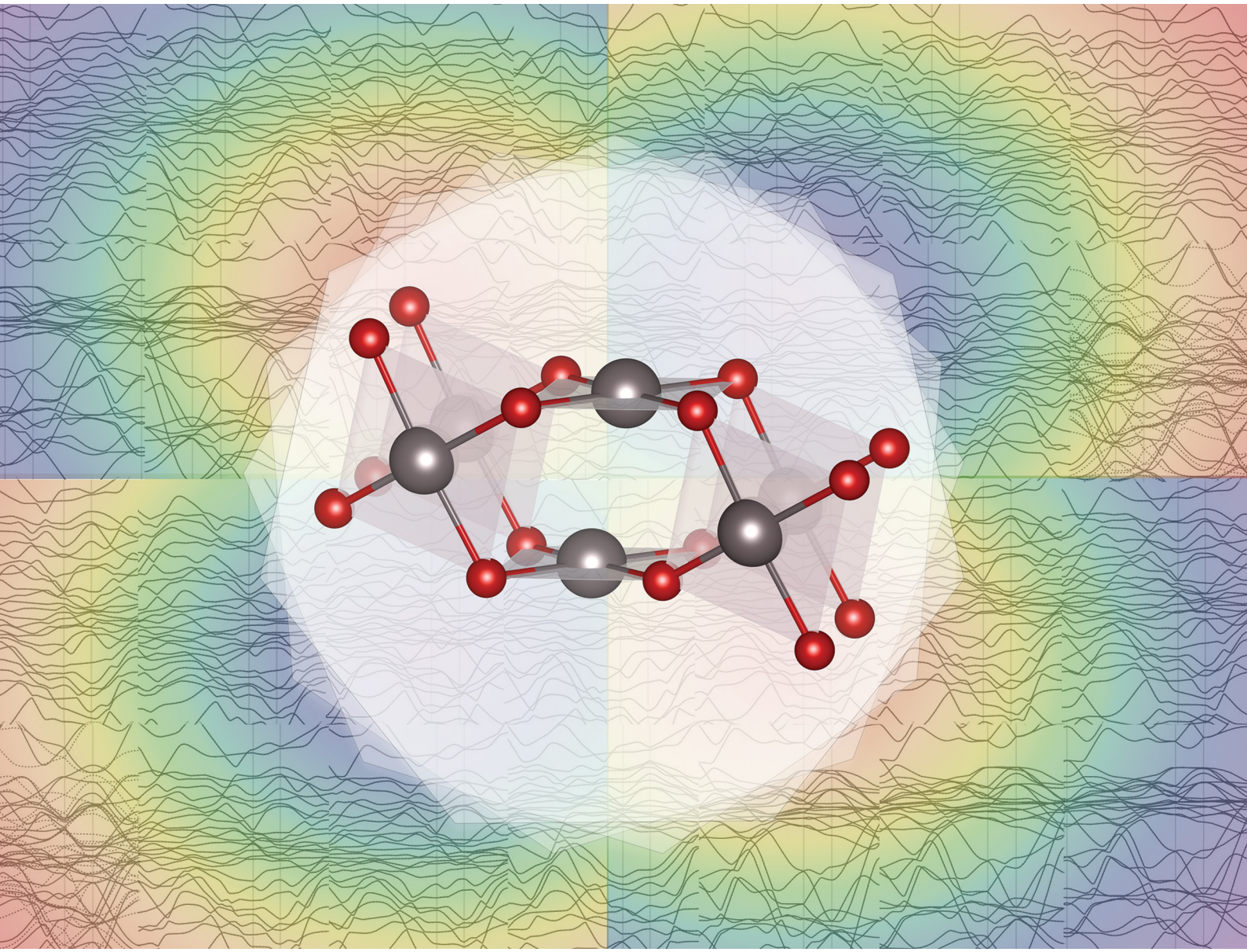

ISSN 1463-9076

ROYAL SOCIETY OF CHEMISTRY

TUTORIAL REVIEW

Bram Hoex *et al.*

Designing 3d metal oxides: selecting optimal density functionals for strongly correlated materials

PCCP

ROYAL SOCIETY OF CHEMISTRY

TUTORIAL REVIEW

View Article Online
View Journal | View Issue

Cite this: *Phys. Chem. Chem. Phys.*, 2022, **24**, 14119

Designing 3d metal oxides: selecting optimal density functionals for strongly correlated materials†

Ina Østrøm, [a] Md. Anower Hossain, [a] Patrick A. Burr, [b] Judy N. Hart [c] and Bram Hoex*[a]

Transition metal oxides (TMOs) have remarkable physicochemical properties, are non-toxic, and have low cost and high annual production, thus they are commonly studied for various technological applications. Density functional theory (DFT) can help to optimize TMO materials by providing insights into their electronic, optical and thermodynamic properties, and hence into their structure–performance relationships, over a wide range of solid-state structures and compositions. However, this is underpinned by the choice of the exchange–correlation (XC) functional, which is critical to accurately describe the highly localized and correlated 3d-electrons of the transition metals in TMOs. This tutorial review presents a benchmark study of density functionals (DFs), ranging from generalized gradient approximation (GGA) to range-separated hybrids (RSH), with the all-electron def2-TZVP basis set, comparing magneto-electro-optical properties of 3d TMOs against experimental observations. The performance of the DFs is assessed by analyzing the band structure, density of states, magnetic moment, structural static and dynamic parameters, optical properties, spin contamination and computational cost. The results disclose the strengths and weaknesses of the XC functionals, in terms of accuracy, and computational efficiency, suggesting the unprecedented PBE0-1/5 as the best candidate. The findings of this work contribute to necessary developments of XC functionals for periodic systems, and materials science modelling studies, particularly informing how to select the optimal XC functional to obtain the most trustworthy description of the ground-state electron structure of 3d TMOs.

Received 18th March 2022,
Accepted 7th May 2022

DOI: 10.1039/d2cp01303g

rsc.li/pccp

[a] *School of Photovoltaic and Renewable Energy Engineering, UNSW, Kensington, NSW 2052, Australia. E-mail: b.hoex@unsw.edu.au*
[b] *School of Mechanical and Manufacturing Engineering, UNSW, Kensington, NSW 2052, Australia*
[c] *School of Materials Science & Engineering, UNSW, Kensington, NSW 2052, Australia*

† Electronic supplementary information (ESI) available. See DOI: https://doi.org/10.1039/d2cp01303g

Ina Østrøm

Ina is a Scientia PhD scholar at UNSW's School of Photovoltaic and Renewable Energy Engineering in Sydney. Her research focusses on the computational design and atomic layer deposition synthesis of low-cost catalysts for 0next-generation H_2 devices. Ina is interested in studying structure-property relations to model materials for different applications with computational tools. She obtained a MSc degree in theoretical chemistry at UFSC in Brazil (2019). Ina is the coordinator of Equity, Diversity and Inclusion (EDI) at the Women's Research Engineering Network (WREN).

Md. Anower Hossain

Md. Anower Hossain is a post-doctoral research fellow in the School of Photovoltaic and Renewable Energy Engineering at the UNSW, Sydney, Australia. He received his PhD degree in Materials Science and Engineering from the National University of Singapore in 2013. His research interests include experimental solar photovoltaics, fuel cells catalysts, and materials modelling using the first-principles density functional theory (DFT) and molecular dynamics (MD) simulations.

1 Introduction

Transition metal oxides (TMOs) are semiconductors that possess a range of physicochemical properties, such as wide band gap, magnetic states, electrical conductivity and metal–oxygen bonding that varies in nature from nearly ionic to highly covalent or metallic.[1–3] The importance of 3d TMOs has been acknowledged in materials science as they can be employed in a wide variety of technologies, *e.g.*, catalysis, biomedical devices, microelectronics, data storage, opto-electronics, thermoelectrics, solar cells, batteries, sensors, supercapacitors, and composites.[4–17] Furthermore, when compared to 4d and 5d TMOs, 3d TMOs are less toxic, cheaper, and more abundant, thus they are strong candidates as environmentally and economically sustainable functional materials.[18,19] From a theoretical viewpoint, 3d TMOs serve as prototype systems to be investigated because of their spin, charge, orbital and lattice degrees of freedom and interactions; these are related to quantum mechanical processes that result in unique electronic properties and orbital degeneracies, that are not predicted or explained by simple models.[20–24] Some examples are relativistic spin–orbit coupling, direct-exchange and super-exchange (ferromagnetic or antiferromagnetic) spin–lattice, orbital–lattice (Jahn–Teller distortion), orbit–orbit and magnetic dipole–dipole interactions, and orbital and magnetic anisotropy.

Rational design and selection of 3d TMO materials for different applications require understanding their atomic composition and electronic structure.[25] Scaling relation descriptor-based investigation of TMOs provides a basis for prediction and tuning of material properties by correlating theoretical models of structural and electronic descriptors with experimental data.[26] Density functional theory (DFT)[27,28] is a powerful and versatile tool that can be used in structure–performance investigation of molecular and solid-state systems, and hence in understanding 3d TMO material properties.[29–34] The usefulness and workflow of employing DFT to design materials is expressed in Fig. 1. The workflow shows the best practices in employing DFT, which begins with the correct choice of the level-of-theory, followed by calculation of ground-state properties, which can be studied as structure–performance descriptors leading to the development of materials with optimized performance for a wide range of technological applications.

High-throughput DFT calculations have facilitated the creation of large databases of DFT-predicted material properties. Some examples are the Open Quantum Materials Database,[35] Materials Project,[36] the Computational Materials Repository,[37] and AFLOWLIB,[38] which allow direct searches of desired descriptors of materials calculated using semi-local GGA density functionals. Only recently has a hybrid DFT database been launched, which is expected to provide more accurate property values than semi-local DFs, but at a higher computational cost.[39] In 2022, Kuklin *et al.* compared the structural and magnetic ground-state properties to experimental data for a collection of 100 binary 3d, 4d, and 5d TMOs.[40] Their DFT calculations employed hybrid DF PBE0,[41,42] and Gaussian-type

Patrick A. Burr

Patrick A. Burr is an atomic scale modeler and a Senior Lecturer in Nuclear Engineering at the UNSW, with a PhD in computational materials science from Imperial College London (2015). His research is centred around understand the degradation processes that occur in materials used for energy applications. In particular, he focuses on materials used in nuclear fission, fusion, hydrogen, photovoltaic and batteries, as these are subject to the most demanding environments.

Judy N. Hart

Dr Judy N. Hart is a Senior Lecturer in the School of Materials Science and Engineering at UNSW Sydney. After completing her PhD in Materials Engineering at Monash University, she was a post-doctoral researcher at the University of Bath and then held a Ramsay Memorial Fellowship in the Centre for Computational Chemistry, University of Bristol. Her research interests are in the combined use of computational (e.g. density functional theory) and experimental approaches to design new semiconductor materials, particularly for renewable energy applications and catalysis.

Bram Hoex

Bram Hoex is a Professor at UNSW Sydney and Deputy Head at UNSW's School of Photovoltaic and Renewable Energy Engineering. His research focusses on the development and application of nanoscale thin films in a wide range of renewable energy devices. He published over 200 scientific papers which have been cited over 7000 times. His work has received various international recognitions including the 2008 SolarWorld Junior Einstein and the 2016 IEEE PVSC Young Professional awards, and he was listed in the "Solar 40 under 40 list" globally by Renewable Energy World in 2018.

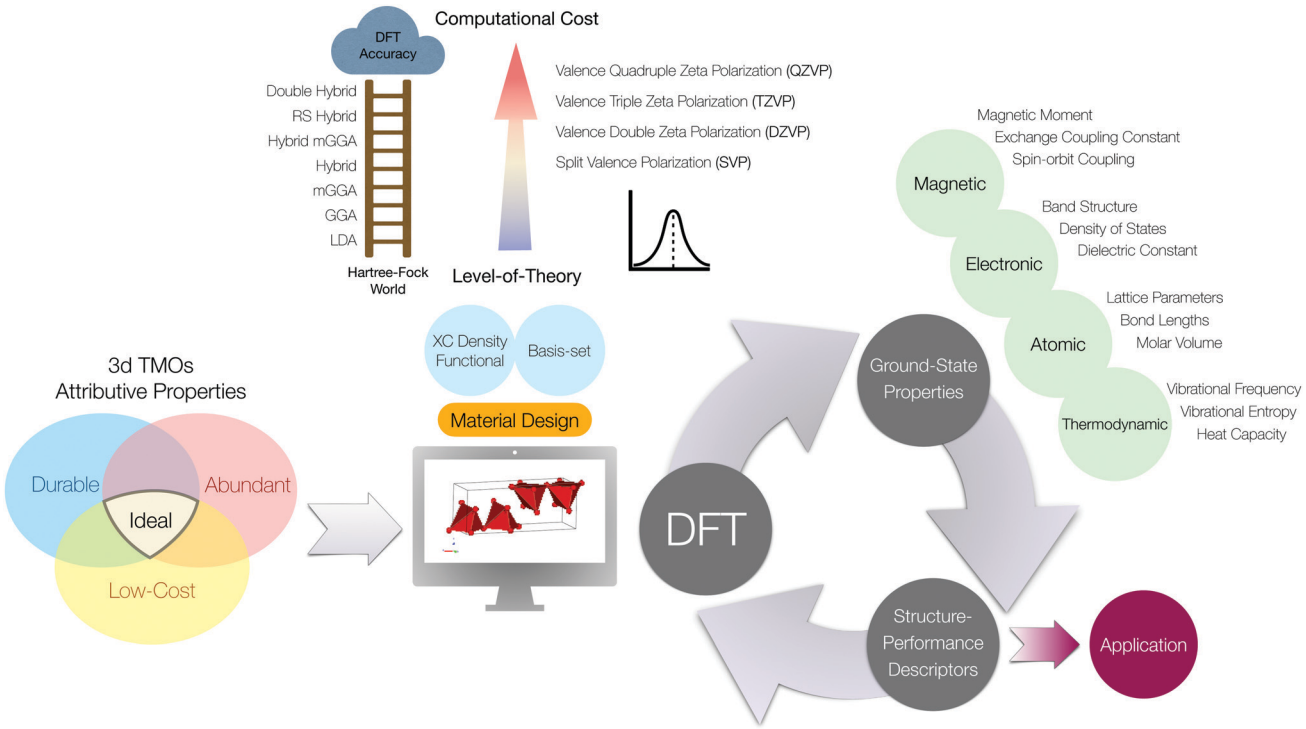

Fig. 1 Workflow illustrating the rational design of materials for different applications. The best practices for employing DFT to model materials requires an informed choice of level-of-theory. The calculated DFT ground-state properties can be correlated with structure–performance descriptors to optimise materials.

localized basis sets, highlighting the need to shift towards hybrid DFT for periodic systems. However, comparison with different DFs is critical to understand their effects on the properties of TMOs and to motivate their optimization to periodic systems.

The correct description of structure–property relations with DFT requires an adequate and informed choice of the level of theory to use, specifically the Hamiltonian density functional (DF) and the atomic orbital basis sets (BS).[43,44] A wise choice of DF and BS to treat a particular class of periodic systems such as 3d TMOs leads to accurate property prediction with reasonable computational cost. Benchmarks, perspectives, and reviews serve to guide new users about the good practices of DFT applications and outline possible avenues for further refinement to existing methods.[45–51]

The inherent limitations of DFT approximations for periodic systems, combined with uninformed comparison of DFT properties to non-standardized experimental data-sets, results in incorrect models and interpretations.[45,52–55] In this regard, when modelling 3d TMOs, we have to be aware of: (i) the localized nature of 3d orbitals in contrast to 4d and 5d TMOs, which makes 3d TMOs strongly-correlated materials;[1] (ii) the self-interaction error (SIE), which is intrinsic to DFT theoretical grounding and leads to a spurious electron–electron repulsion;[23,56,57] (iii) and the concomitant self-interaction delocalization error, which results in incorrect fractional charges, complications with activation energy barrier heights in reactions, underestimation of band gaps, and underestimation of excited-state energies.[58,59] Attempts to fix some pitfalls of DFT led to the development of newer XC functionals, such as hybrid DFs that include a percentage of Hartree–Fock (HF) exchange globally, and/or use of some screened range-separation.[60] Unfortunately, these functionals are computationally demanding, which hinders their use for larger TMO systems (*e.g.* 200 atoms), and some lack theoretical foundation for their apparent accuracy (*e.g.* accuracy is achieved fortuitously through cancellation of errors).[46] Hence, the semi-local generalized gradient approximation (GGA) DF is the most used method in descriptor-based materials design because of its simplicity, computational efficiency, and reliability for some properties, regardless of its inadequacy in describing the band structure of semi-conductors and insulators.[60–62]

The infinite nature of the periodic boundary conditions in solid-state systems suggests the employment of plane wave (PW) basis functions as basis sets to expand Bloch orbitals.[31] Indeed, the majority of periodic DFT codes available are based on such delocalized functions. The advantage of PW lies in the absence of basis set superposition error, because the basis set is independent of nuclear positions. However, the construction of the energy density matrix and full diagonalization of the Hamiltonian is only efficient by approximation, since PW basis sets are composed of several thousand functions.[63] The major shortcomings of delocalized PWs for describing 3d electrons arise due to: (i) the localized nature of 3d orbitals, and (ii) their high computational cost when hybrid DF are required.[64–66] Thus, in this work, all-electron localized basis sets are used.

The myriad DFs available, and the different choices offered by DFT codes and methods,[67,68] hinder efficient and appropriate

choices, even suggesting the need for a broader discussion addressing DFT challenges for solid-states systems, as was done by Cohen and coworkers in the past for molecular systems.[69] Thus, the question we aim to answer is: which density functional offers the best performance, both in terms of accuracy and computational cost, for common properties of 3d TMOs? In this work, we provide a XC functional benchmark overview, with all-electron localized basis set, over a selected range of properties relevant to the design and selection of 3d TMOs for a variety of applications. The analyzed structures include a mixture of open- and closed-shell TMOs: CoO, Cr_2O_3, CuO, Fe_2O_3 (hematite), MnO, NiO, V_2O_3, Cu_2O, TiO_2 (rutile), V_2O_5 and ZnO. The choice of the 3d TMOs was based on their inherent attributive properties, known technological applications, and varied geometry and electronic structures. We examine the DFs performance for describing the (i) structural, (ii) vibrational, (iii) electronic, and (iv) magnetic properties. Beyond simply comparing DFT results to experimental data, we make some theoretical remarks regarding the ground-state DFT properties, and what are the best practices in deciding which DF to use. The last section gives the DFs overall performance on the properties analysed, suggests a novel DF recipe with highest overall accuracy, and provides the average computational cost for each DF. This DF benchmark study aims to facilitate future modelling of 3d TMOs in terms of making an informed and wise choice of DFT level of theory for calculating properties of different TMOs for various applications, and to inspire further uplift of DFT in the solid-state community.

2 Computational methodology

DFT calculations were performed with the CRYSTAL17 code.[70–72] To avoid basis set superposition error (BSSE), all calculations were performed with relativistic balanced all-electron triple-ζ valence with polarization (TZVP) basis sets from the Karlsruhe def2 family.[44] Relativist effects were not considered, as the spin–orbit coupling (SOC) correction is not yet implemented in CRYSTAL17, although it is under development.[73]

The XC functionals discussed in this work are classified in Table 1 in terms of the type of exchange (X) and correlation (C) functionals, the amount of Hartree–Fock (HF) exact exchange E_{HF}, and the short-range ($\omega_{SR}(r)$) and long-range ($\omega_{LR}(r)$) Coulomb screening length scales.

The choice of the DF follows Perdew's concept of the "Jacobs ladder".[43,74] Each rung introduces a different level of approximation, by adding a parameter to the previous rung, in order to ameliorate the XC functionals accuracy. Thus, the "ladder" can be climbed towards higher dependency on $\rho(r)$ and hence more accurate results, although with the trade-off of increased computational demand. According to the DF availability in CRYSTAL, and varying E_{HF} from 0% (lowest) to 60% (highest), the DFs investigated in this work were: GGA functionals PBE,[75] PBESOL,[76] and BLYP,[77,78] the meta-GGA (mGGA) M06L,[79] the global hybrids B3LYP,[80] B3PBE,[75,80] B3PW,[80,81] PBE0,[41,42] PBE0-1/3,[82] and PBESOL0,[41,76] the hybrid mGGA (HmGGA) M06,[83] and finally the range-separated hybrids (RSH) HSE06,[75,84] HSESOL,[76,85] and HISS.[86,87]

The crystallographic structures of the TMOs were obtained from the Inorganic Crystal Structure Database (ICSD): CoO,[88] Cr_2O_3,[89] CuO,[90] Fe_2O_3,[91] MnO,[92] NiO,[92] V_2O_3,[93] Cu_2O,[94] TiO_2,[95] V_2O_5,[96] and ZnO.[97] The crystallographic structure details and illustrations can be found in the ESI.† The unrestricted Kohn–Sham (UKS) approach was used for the spin-polarized TMOs CoO, CuO, Cr_2O_3, Fe_2O_3, MnO, NiO, and V_2O_3. For these open-shell systems, the AFM-II magnetic configuration, which is their configuration below the Néel temperature (T_N), was used: CoO (291 K), CuO (230 K), Cr_2O_3 (318 K), Fe_2O_3 (948 K), MnO (122 K), NiO (525 K), and V_2O_3 (150 K).[98–101] The AFM-II spin ordering structures are illustrated in Fig. S4, and given in the input section in the ESI.†

Grimme's D3 empirical dispersion correction was used for the V_2O_5 layered structure with Becke–Johnson damping (BJ),[102,103] except for the HISS DF, for which D3-BJ parameters were not available. The D3-BJ scheme for dispersion corrections is the only available in CRYSTAL17, however many-body dispersion effects may be more adequate for periodic systems and layered structures.[104–106] An $8 \times 8 \times 8$ k-points mesh was used for geometry optimization and coupled perturbed Kohn–Sham (CPKS) calculations of all structures.[107–109] In all calculations, truncation tolerance factors for the Coulomb and exchange

Table 1 Classification of density functionals used in this work according to the type of exchange (X) and correlation (C) functional, amount of exact exchange (E_{HF}), and short-range ($\omega_{SR}(r)$) and long-range ($\omega_{LR}(r)$) length scales ($r = a_0^{-1}$)

Density functional	Type	Exchange	Correlation	E_{HR} (%)	ω_{SR} (r)	ω_{LR} (r)
PBE	GGA	PBE	PBE	0	0	0
BLYP	GGA	BECKE	LYP	0	0	0
PBESOL	GGA	PBESOL	PBESOL	0	0	0
M06L	meta-GGA	M06L	M06L	0	0	0
B3PW	Global hybrid	BECKE3	PW	20	0	0
B3PBE	Global hybrid	BECKE3	PBE	20	0	0
B3LYP	Global hybrid	BECKE3	LYP	20	0	0
PBE0	Global hybrid	PBE	PBE	25	0	0
PBESOL0	Global hybrid	PBESOL	PBESOL	25	0	0
PBE0-1/3	Global hybrid	PBE	PBE	33.3	0	0
M06	Hybrid meta-GGA	M06	M06	27	0	0
HSE06	Range-separated hybrid	SC-PBE	PBE	25	0.11	0.11
HSESOL	Range-separated hybrid	SC-PBESOL	PBESOL	25	0.11	0.11
HISS	Range-separated hybrid	HISS	PBE	60	0.84	0.20

integrals were set to 10^{-8} for the overlap threshold of Coulomb integrals, 10^{-8} for the penetration threshold of Coulomb integrals, 10^{-8} for the overlap threshold of HF exchange integrals, and 10^{-8} and 10^{-16} for pseudo-overlap in the HF exchange series.

Geometry optimization of the TMO structures was performed allowing both atom positions and lattice parameters to be fully relaxed without symmetry constraints. The total energy convergence criterion of $10^{-8}E_h$, with the default integration grid. For harmonic vibrational frequency calculations at the Gamma (Γ) point, the total energy convergence threshold was increased to $10^{-10}E_h$. Analysis of the eigenvalues was done to check whether the optimized structures correspond to true minima. Denser k-point meshes were used for band structure ($16 \times 16 \times 16$) and density of states (DOS) ($32 \times 32 \times 32$) calculations, to produce accurate well-defined plots. The wave vectors of the Brillouin zone paths were determined based on Setyawan's work.[110]

The accuracy of the calculated values was evaluated in terms of the dimensionless relative approximation error δ_{approx}, defined as

$$\delta_{approx} = 100 \times \left[\frac{(x_{exp} - x_{DFT})}{x_{exp}}\right] \quad (1)$$

Hence, overestimations ($x_{DFT} > x_{exp}$) and underestimations ($x_{DFT} < x_{exp}$) have negative and positive δ_{approx} values, respectively.

The overall performance evaluation of the DFs was based on the average of the absolute approximation error (δ_{avg}), defined by:

$$\delta_{avg} = \frac{1}{n}\sum_{n} |\delta_{approx}| \quad (2)$$

where n is the number of δ_{approx} considered.

3 Results and discussion

3.1 Structural properties

To ascertain the performance of the DFs for predicting the structural parameters of TMOs, we compare the optimized bulk density ρ_{bulk} against experimental measurements, for which there is an abundance of precise reports in the literature. The relative approximation errors (δ_{approx}) are presented in Fig. 2 as a colormap. The linear color scale was set considering the maximum absolute value of δ_{approx}, varying from blue, indicating overestimation relative to the experimental ρ_{bulk} values, to red indicating the underestimation. The most accurate ρ_{bulk} are values colored in yellow (*i.e.* indicating relative approximation errors that are closest to zero). The average of the absolute approximation errors δ_{avg} (bottom row), and experimental values (right column), are also provided. Similar colormaps for the calculated lattice parameters a with the corresponding

	GGA			mGGA	Global Hybrid						Hybrid mGGA	Range-Separated Hybrid			
TMO	BLYP	PBE	PBESOL	M06L	B3PW	B3PBE	B3LYP	PBE0	PBESOL0	PBE0-13	M06	HSE06	HSESOL	HISS	ρ_{bulk}
CoO	3.59	-3.96	-9.69	-0.54	0.59	-1.01	3.29	0.26	-3.40	-0.09	-1.15	0.20	-3.45	-0.73	6.43
CuO	13.05	9.36	4.73	0.09	3.61	-0.44	9.70	-0.11	-5.19	-1.91	7.11	0.11	-4.98	-3.55	6.34
Cu_2O	5.71	0.72	-4.68	-0.65	0.51	-1.52	4.20	0.02	-3.91	-0.12	0.67	0.00	-3.96	-0.56	5.85
Cr_2O_3	5.64	2.68	-1.41	3.14	1.51	0.36	3.67	1.03	-1.53	0.38	2.05	1.07	-1.51	0.06	5.18
Fe_2O_3	4.29	0.90	-5.13	1.59	1.03	-0.10	3.29	0.46	-2.54	-0.31	1.05	0.50	-2.05	-0.84	5.20
MnO	3.02	-0.37	-5.18	0.13	0.11	-1.44	2.39	-0.32	-3.52	-1.21	0.07	-0.37	-3.50	-1.14	5.39
NiO	5.35	1.35	-3.92	2.09	1.02	-0.53	3.80	0.67	-3.06	0.27	2.32	0.65	-3.02	-0.50	6.69
V_2O_5	14.81	19.80	9.09	6.13	11.64	12.86	9.87	6.97	2.93	6.07	3.50	6.49	3.02	-23.15	3.34
V_2O_5*	3.86	6.34	1.53	4.82	-11.64	-12.14	-7.81	-6.94	-9.54	-8.20	0.09	-8.20	-9.63	N/A	3.34
V_2O_3	3.43	0.04	-4.70	1.10	2.03	0.84	4.26	1.73	-0.82	1.39	2.73	1.69	-0.92	1.25	4.90
ZnO	6.94	3.96	-0.30	2.38	1.74	0.43	3.98	1.15	-1.83	0.36	0.47	1.27	-1.72	-0.48	5.51
TiO_2	4.30	1.74	-1.34	0.71	-0.85	-1.83	1.06	-1.55	-3.64	-2.51	-0.61	-1.48	-3.60	-2.96	4.32
δ_{avg}	6.16	4.27	4.31	1.95	3.02	2.79	4.78	1.77	3.49	1.90	1.82	2.00	3.45	3.20	

Over
Under

Fig. 2 Relative approximation errors in calculated bulk density (ρ_{bulk}) values, color-coded by the relative difference from experimental values in g cm^{-3} (right column). V_2O_5* includes D3-BJ corrections. References for experimental values are available in the ESI.†

δ_{approx} and calculated values of ρ_{bulk} can be found in Fig. S7 of the ESI.†

The accuracy in predicting ρ_{bulk} by the different XC functionals can be ascertained by the δ_{approx} colors. For example, there is a slight tendency of BLYP and B3LYP to underestimate ρ_{bulk} (indicated by red shades in these columns), while the XC functionals designed for periodic systems, PBESOL, PBESOL0 and HSESOL, tend to overestimate ρ_{bulk} (shades of blue). The accuracy of the ρ_{bulk} with the global hybrids B3PW, B3PBE, PBE0 and PBE0-1/3 (light yellow) is significantly better when compared to B3LYP and PBESOL0. The underperformance of B3LYP may be due to the incorrect part of the correlation functional in the homogeneous electron gas threshold, as reported previously.[111]

M06L, B3PBE, PBE0, PBE0-1/3, M06, and HSE06 exhibit the least deviation from experimental values ($\delta_{avg} < 3\%$), with PBE0 and M06 providing close agreement for most TMOs (PBE0 with less than 2% error for all except V_2O_5). For most TMOs, the mGGA M06L provided a substantial improvement over the GGA functionals, and several hybrids, although the δ_{avg} of the pure GGA PBE was better than the hybrid B3LYP.

V_2O_5 has a layered structure, so the density was calculated with (V_2O_5*) and without (V_2O_5) dispersion corrections. With no dispersion consideration, ρ_{bulk} tends to be underestimated, with the exception of HISS, which greatly overestimates it by 23.2%. The poor description of V_2O_5 using HISS is surprising given that it is an RSH functional, and it is chiefly due to underestimation of approximately 10.9% in *a* and 14.6% in *b*, couple with an overestimation of *c* by 6.7%. The addition of the D3-BJ dispersion correction for V_2O_5* consistently increases the density, leading to a shift from underestimation (red) to overestimation (blue). However, in most cases, the magnitude of the error is less when the D3-BJ dispersion correction is applied, with the notable exceptions of PBE0-1/3 (2.1% increase in error magnitude), HSE06 (1.7%), PBESOL0 (6.6%) and HSESOL (6.6%). The latter two cases are DFs specifically optimized for periodic systems, thus their parameterization may implicitly account for some of the larger volumes of layered structures, making the D3 correction unnecessary and inappropriate. In fact, it has been reported that the use of Heyd–Scuseria–Ernzerhof (HSE) range-screened scheme to reduce SIE is useful to account for dispersion corrections.[112]

The accuracy in ρ_{bulk} is critical to predicting other material properties. For instance, for strongly correlated systems like CoO, CuO, Cr_2O_3, Fe_2O_3, MnO, NiO, and V_2O_3, ρ_{bulk} reflects how capable the XCs are for describing spin–lattice interactions.[98–101] In these open-shell TMOs, antiferromagnetic spin ordering of type AFM-II occurs below the Néel temperature, and magnetic driven Jahn–Teller distortions occur, mainly affecting cell angles, due to direct and super-exchange effects that arise from orbital interactions between the anion and the cation electronic sub-systems.[23,113] The semi-local PBESOL has the largest overestimated values of ρ_{bulk} for the cubic structures: CoO (9.7%) > MnO (5.2%) > NiO (3.9%). Interestingly, their deviation from orthogonal crystallographic angles follows the same order, *i.e.*, CoO (96.3°) > MnO (91.9°) > NiO (90.4°), indicating that poor structural description can be related to difficulties in describing the open-shell systems.

3.2 Lattice dynamics

Harmonic vibrational frequencies at the Γ point were obtained by calculating the numerical derivatives of finite displacements of the atomic positions in the Hessian matrix.[114,115] Comparison to experimental data was done through selected vibrational modes that are either infrared (IR) or Raman active, for which the approximation errors δ_{approx} and average absolute errors δ_{avg} are presented in Fig. 3. Analysis of harmonic frequencies at the Γ point only is sufficient for comparison to experimental IR and Raman results[116,117] and allow exploration of the DFs numerical accuracy and evaluation of their differences in describing bond forces,[118] while being much less computationally demanding than phonon dispersion calculations, which require large supercells.

A table of the vibrational modes and frequencies (cm^{-1}) for all TMOs, with corresponding references (Table S1, ESI†), and a colormap of the calculated values (Fig. S8) can be found in the ESI.† Table S2 (ESI†) shows which combinations of DFs and TMOs had negative eigenvalues and imaginary frequencies. The vibrational frequency analysis reflects the shape of the potential energy surface, specially around the minimum. The absence of negative eigenvalues of the Hessian second derivative indicate that the optimized ground-state structure corresponds to a local or global minima.

The optimized structures that were found to have imaginary frequencies, V_2O_5 and TiO_2, are either unstable due to intrinsic factors related to the atomic and electronic structures or the result may indicate some difficulty for the XC functional to yield the global minimum structure. Phonon frequency evaluation, even solely at the Γ point is very demanding. For the TMO cells of Cr_2O_3 and V_2O_3, calculations with RSH were too expensive, and the force constant matrix numerical estimation did not finish. For CoO calculated with M06, the N/A in Table S2 (ESI†) indicates a zero determinant in the mass-weighted dynamical matrix of the Hessian analysis.

We can see from the shades of colors in Fig. 3 that all the XC functionals give good agreement with experimental data (indicated by pale yellow shades), with a slight tendency of GGA and mGGA to underestimate (pale red) the frequencies, and some global hybrids (PBESOL and PBE0-1/3) and RSH (HSESOL and HISS) to overestimate them. Higher δ_{approx} overestimations are seen for CoO for all XC functionals other than GGA functionals, with the highest values given by HSESOL < PBESOL0 < PBE0-1/3. Interestingly, large underestimations were obtained for MnO with the GGA functionals (dark red). The average of the absolute δ_{approx}, given by δ_{avg}, indicate that overall the most accurate DFs ($\delta_{avg} < 5\%$) for predicting vibrational frequencies are: M06 < B3PBE < B3LYP < B3PW < PBE0 < HSE06. B3PW, PBESOL, and HISS have the lowest number of TMOs with negative values in the Hessian matrix (Table S2, ESI†), B3LYP has the most followed by HSE06, and HSESOL, both of which have prohibitive computational costs for Cr_2O_3 and V_2O_3, together with HISS.

	GGA			mGGA	Global Hybrid						Hybrid mGGA	Range-Separated Hybrid			
TMO	BLYP	PBE	PBESOL	M06L	B3PW	B3PBE	B3LYP	PBE0	PBESOL0	PBE0-13	M06	HSE06	HSESOL	HISS	ω_ν
CoO	-1.71	0.95	8.35	-8.21	-7.70	-11.26	-2.19	-11.22	-16.39	-23.88	N/A	-10.12	-16.19	-13.69	350
CuO	13.22	10.04	5.06	9.06	-2.72	-3.36	-1.50	-2.33	-5.28	-1.94	-3.54	-2.01	-4.96	-3.45	530
Cu_2O	10.32	4.52	-2.44	-0.36	2.99	0.37	7.32	2.11	-3.00	1.64	2.86	2.19	-2.96	0.26	634
Cr_2O_3	8.34	8.07	6.68	4.99	1.41	1.19	1.61	0.15	-0.96	-1.99	0.28	N/A	N/A	N/A	444
Fe_2O_3	8.94	7.26	6.94	-3.20	-2.03	-3.12	-0.93	-3.62	-5.01	-6.25	-3.33	-3.31	-6.00	-7.21	408
MnO	51.13	39.18	42.76	28.83	3.86	1.06	10.25	-2.42	-6.58	-9.43	5.84	-1.09	-5.41	-12.01	258
NiO	10.95	4.24	-3.41	-1.60	-3.79	1.33	1.65	-6.05	-12.55	-8.20	-1.71	-5.81	-12.20	-9.26	387
V_2O_5	15.60	17.10	11.21	15.25	2.51	-3.23	-0.25	-3.30	-4.43	-4.86	-2.76	-2.76	-4.16	-4.50	506
V_2O_3	8.21	4.46	-0.84	5.64	2.05	0.18	-2.18	0.52	-3.05	-1.46	2.17	N/A	N/A	N/A	501
ZnO	5.97	2.16	-3.97	-2.52	-3.51	-5.49	-0.52	-4.96	-9.41	-7.03	-1.00	-4.73	-9.11	-8.16	407
TiO_2	8.50	5.94	2.14	0.52	1.13	-0.18	2.93	-0.40	-3.10	-2.49	2.12	-0.19	-2.89	-3.51	612
δ_{avg}	12.99	9.45	8.53	7.29	3.06	2.80	2.85	3.37	6.34	6.29	2.56	3.58	7.10	6.90	

Fig. 3 Relative approximation errors in calculated harmonic phonon vibration frequency (ω_ν) at the Γ point, color-coded by the relative difference from experimental values (right-hand column); average absolute errors δ_{avg} are given in the bottom row. References for experimental values are available in the ESI.†

Comparing the δ_{avg} values for the vibrational frequencies revealed minor differences between the DFT functionals, which is why simple DFT methods such as GGA and mGGA functionals can reasonably predict structural parameters, and commensurately predict other thermodynamic derived data, such as surface and adsorption energies, heat capacity, and vibrational entropy.[119–121] Not surprisingly, GGA are the most used DFs for modelling systems with a large set of atoms, especially those including metals, due to its computational efficiency.

3.3 Band structures and densities of states

The band gap (E_g) approximation errors for all TMOs calculated with the range of XC functionals studied are given in the colormap in Fig. 4. A colormap with the DFT calculated values, containing the references to the experimental data, is available in the ESI† (Fig. S9).

The different colors in the columns of Fig. 4 show a clear and noted trend of E_g values for the different rungs of XC functionals. The GGA functionals, which have no E_{HF} exchange contribution, result in significant underestimation of the E_g for all TMOs, varying between 47% and 88%, except for V_2O_5, (22–26% underestimation), which might foreshadow an attenuation of exchange effects in layered structures. TMOs possessing an odd number of d electrons are expected to be Mott insulators with antiferromagnetic ordering, due to SOC effects.[122] Thus, the convergence to metallic states for CoO and CuO with GGA, which is in clear disagreement with the experimental E_g values of 2.60 and 1.70 eV, respectively, is due to the inability of GGA functionals to correctly describe electronic interactions.[123–127] For other TMOs, such as the closed-shell Cu_2O and open-shell Fe_2O_3, which have experimental E_g of 2.17 and 2.20 eV respectively, the semi-local DFs were able to correctly predict an energy gap, although it is still strongly underestimated ($\sim$78% for Cu_2O, and $\sim$89% for Fe_2O_3).[128,129]

Climbing up to the third rung of DFs, progress up to $\sim$30% in E_g prediction are obtained comparing GGA to mGGA, especially in the case of the open-shell systems, despite mGGA still having no E_{HF} exchange contribution. In contrast to GGA, mGGA M06L correctly predicted CoO and CuO to be semiconductors, albeit with a large underestimation in E_g of 87.6% for CoO and 78.4% in CuO. For these AFM-II monoxides, this can be related to mGGA better relative stability of the magnetic orderings. The inability to converge to the correct insulating state may be associated with difficulties in obtaining the correct ground-state electron configuration due to the 3d orbital degeneracy. For the cubic octahedral TMOs CoO, NiO and MnO, we calculated the exchange energy per formula unit (ΔE_X) as the energy difference between the ferromagnetic (FM) and AFM-II magnetic structures (Table S3, ESI†). The rock salt CoO structure optimized with M06 yields an FM spin configuration that is 44.6 meV more stable than AFM-II (Table S3, ESI†). With GGA BLYP, PBE and PBESOL, the AFM-II

	GGA			mGGA	Global Hybrid						Hybrid mGGA	Range-Separated Hybrid			
TMO	BLYP	PBE	PBESOL	M06L	B3PW	B3PBE	B3LYP	PBE0	PBESOL0	PBE0-13	M06	HSE06	HSESOL	HISS	E_g
CoO	N/A	N/A	N/A	87.55	-38.39	-35.81	-39.42	-71.84	-63.95	-115.13	N/A	-42.49	-33.58	-96.40	2.60
CuO	N/A	N/A	N/A	78.38	-48.65	-52.49	-11.96	-100.39	-94.36	-149.00	-55.29	-57.53	-51.91	-120.77	1.70
Cu_2O	78.42	79.35	75.82	73.28	10.80	11.23	9.45	-6.48	-9.34	-39.26	-8.52	17.57	14.43	-22.61	2.17
Cr_2O_3	61.64	62.65	69.58	39.84	-24.87	-24.17	-25.43	-46.88	-42.24	-83.12	-31.57	-25.74	-20.94	-63.24	3.40
Fe_2O_3	84.90	85.27	97.61	42.01	-37.26	-37.49	-35.17	-69.79	-65.21	-123.77	-60.85	-37.60	-33.93	-83.57	2.20
MnO	65.06	69.17	68.87	61.36	5.95	7.22	3.72	-6.93	-8.94	-35.17	-7.18	11.73	10.37	-22.30	3.60
NiO	77.30	77.47	82.11	52.18	-0.79	-1.45	1.10	-21.76	-19.90	-50.51	-6.18	-4.97	-2.83	-33.83	4.30
V_2O_5	24.35	21.77	22.61	11.11	-10.28	-10.44	-9.74	-25.92	-25.35	-52.64	-24.39	-2.01	1.20	-31.36	2.30
V_2O_5*	26.60	23.09	24.70	11.37	-7.58	-8.14	-6.06	-22.78	-7.95	-49.56	-21.60	0.37	0.23	N/A	2.30
ZnO	62.43	64.20	65.57	55.23	3.26	4.66	3.71	-11.07	-10.13	-38.03	-0.62	8.92	9.71	-24.79	3.20
TiO_2	48.67	47.48	47.27	38.74	-5.38	-5.82	-4.19	-20.02	-19.92	-45.00	-17.97	1.33	1.47	-22.12	3.30
δ_{avg}	63.13	63.58	66.44	53.99	18.29	18.85	14.02	37.79	34.19	72.85	23.31	20.82	17.94	54.40	

Fig. 4 Relative approximation errors in band gap E_g (eV), color-coded by the relative difference from experimental values (right-hand column); average absolute errors δ_{avg} are given in the bottom row. Conducting metallic states (N/A) were obtained for CoO and CuO. V_2O_5* includes D3-BJ corrections. References for experimental values are available in the ESI.†

is more stable, hence the metallic states are probably due to incorrect prediction of electron distribution of the ground-state. CuO is the only monoxide for which the AFM-II spin ordering results in an asymmetric monoclinic structure due to strong spin–lattice coupling.[130] The narrow band gap and high electron correlation make it more difficult for semi-local DFs to describe the occupied d^9 orbitals.

Underestimations of E_g for layered V_2O_5* are significantly lower with BLYP (26.6%), PBE (23.1%), PBESOL (24.7%) and M06L (11.4%), when compared to the other TMOs with pure DFT. However, the reduced δ_{approx} are not due to inclusion of the D3-BJ pair-wise dispersion corrections, as it can be seen from the upper row for V_2O_5 that not including D3-BJ corrections gives similarly low δ_{approx} (24.4% for BLYP, 21.8% for PBE, 22.6% for PBESOL, and 11.1% for M06L). Thus, understanding how XC functionals describe layered TMOs structures and why the E_g of layered V_2O_5 is determined with relatively high accuracy with semi-local DFs may be an interesting topic for a future study.

From GGA and mGGA to the global hybrids and advanced RSH methods, we observe three interesting effects on E_g that are related to: (i) the addition of E_{HF} in the hybrids and RSH, (ii) consideration of $\omega(r)$ length-scale to screen the inter-electronic Coulomb operator in RSH, and (iii) small differences due to the XC functional recipes used. The latter refers to DFs such as B3LYP, B3PW, and B3PBE, which all have 20% E_{HF}, but differ in their correlation functionals, being LYP, PW and PBE, respectively.

In general, the addition of 20% E_{HF} and the use of Becke's three parameter scheme (B3)[80] in B3PW, B3PBE, and B3LYP result in the lowest δ_{approx} of the band gaps for all TMOs and DFs. In contrast to pure DFT, δ_{approx} for these three hybrids is not systematic, *i.e.*, the prediction of E_g ranges from under and overestimations. This can be seen comparing δ_{approx} of E_g for BLYP (always underestimates E_g) to B3LYP (varies between under and overestimation). When the amount of E_{HF} is increased from 20% in B3PW, B3LYP, and B3PBE, to 25% in PBE0 and PBESOL0, and then to 33.3% in PBE0-1/3, the band gaps tend to become systematically overestimated. For CuO, increasing E_{HF} from 25% in PBE0 (−100.4%) to 33.3% in PBE0-1/3 (−149%) increases E_g overestimation by almost 49%, while for Fe_2O_3 the overestimation increases by approximately 54% (from −70% with PBE0 to −124% with PBE0-1/3). This suggests that adding 20% of E_{HF} to global hybrids may be a reasonable amount of exchange to optimize results for most 3d TMOs.

Moving to the next higher rung, the hybrid mGGA M06 with 27% of E_{HF}, the addition of $\nabla^2\rho(r)$ and $\tau(r)$ to the XC potentials gives a better δ_{approx} when compared to the 25% E_{HF} in PBE0 and PBESOL0. Nevertheless, comparing M06 to the 20% E_{HF} B3PW, B3PBE and B3LYP, the mGGA still underperforms, which contradicts the expectation based on Jacob's ladder, indicating that 27% E_{HF} exchange is still excessive, and the

addition of a second gradient is not enough to correct it. One should note that M06 fails to obtain a band gap for CoO, but this seems to be an outlier.

The HSE06 and HSESOL, with 25% E_{HF} and the inter-electronic Coulomb potential in E_{HF} weighted with a short-range length scale (ω_{SR}), give striking advances compared to global hybrids PBE0 and PBESOL0, with the same amount of E_{HF}. Furthermore, HSE06 and HSESOL show some advances compared to the hybrid mGGA M06, but in contrast to the latter, both RSH are not systematic in predicting E_g. The two RSH have similar performance in predicting E_g to the 20% E_{HF} global hybrids B3PW, B3PBE, and B3LYP, which comes as a surprise since they should be more accurate and also have higher computational cost. They do improve E_g for some TMOs, for example, in V_2O_5*, both HSE06 and HSESOL show remarkably low values of δ_{approx} for E_g of 0.37% and 0.23%, respectively. The effects on E_g estimation of accounting for mid-range interactions can be seen from the HISS results. Even though HISS has 60% of E_{HF}, which might be expected to result in a massive overestimation of E_g, this is not the case. This can be seen, for instance, comparing the E_g calculated with HISS and PBE0-1/3 – the former has almost twice the amount of E_{HF} compared to the latter, but it considers mid-range interactions, resulting in lower δ_{approx} for all TMOs.

The best performance in terms of accuracy for predicting E_g of 3d TMOs, with δ_{avg} below 25% discrepancy follows: B3LYP < HSESOL < B3PW < B3PBE < HSE06 < M06. Due to the effects observed with adding different amounts of E_{HF}, it would be interesting to investigate E_g calculated with the PBE0 family of hybrids, mGGA M06, and RSH but with E_{HF} reduced to 20% to see if δ_{approx} are lowered without loss in accuracy in predicting structural parameters, for example. Moreover, the variance in δ_{approx} for the different TMOs with different numbers of 3d electrons and unpaired electrons implies that optimization of % E_{HF} may be system dependent, as Seo *et al.* previously observed.[131]

Fig. 5 and 6 show the band structures of selected closed and open-shell TMOs, respectively, plotted over the selected paths of the wavevector $\vec{k}$ in the Brillouin zone, in order of increasing E_{HF} exchange in the DF. Similar illustrations for all other TMOs can be found in Fig. S10–S12 (ESI†). The band structures accompanied by atom projected DOS for all TMOs and functionals are provided in the ESI† (Fig. S13–S23). The electronic levels in TMOs are described by the band structure, with the Fermi level (E_F) defining the boundary between the occupied (valence orbitals) and empty levels (conduction orbitals).[132]

The valence band states are formed by the TM–O bonding electrons and conduction band states are formed by the TM–O antibonding electrons, so that stronger TM–O bonds have decreased interatomic distances, and correspond to higher energy gaps, as the antibonding empty orbitals become higher in energy and the bonding are more stabilized. Band dispersion (difference in energy between the bottom and top of each band) is determined by how orbitals are interacting: weak orbital overlap produces small dispersion (narrow bandwidth), and strong overlap yields a large band dispersion (broad bandwidth). The valence and conduction bands in TMOs with O_h regular octahedral symmetry (*e.g.* MnO, CoO, and NiO (Fig. S10, ESI†)) arise from the oxygen p_x, p_y, and p_z orbitals interacting with the metal t_{2g} (d_{xy}, d_{yz}, d_{zx}) and e_g (d_{z^2}, $d_{x^2-y^2}$) orbitals, and should produce similar band shapes with different DFs.

For most closed-shell TMOs, presented in Fig. 5, the shape of the bands are similar, which confirms that the TM–O bonding calculated with different DFs is similar. The only exception is V_2O_5 calculated with the HISS functional, which lacks the D3-BJ corrections that were applied to all other XC functionals. In this particular case of V_2O_5 with HISS, the bands are very narrow but also separate from each other; since it was seen that ρ_{bulk} is overestimated in this case, these differences in the band structure compared with other DFs may be due to an incorrect description of the layered structure. The V_2O_5 band structures calculated with BLYP, PBE, PBESOL and M06L are somewhat different compared to those calculated with other DFs. From $\Gamma \rightarrow X$ for these DFs, there is less dispersion in the valence bands, whereas, band dispersion increases with increasing E_{HF}. For the other two closed-shell TMOs shown in Fig. 5, the E_g also increases as the amount of E_{HF} in the XC functional increases, but band dispersion and how they run does not change much with different DFs.

The atomic number trends across the 3d series are such that more electrons are distributed in more localized 3d orbitals, which increases electronic repulsion effects. In cases such as in $3d^7$ (CoO) and $3d^9$ (CuO), this leads to even stronger electron exchange and correlation effects originating from the odd unpaired spins in these open-shell TMOs, and SOC effects that can split degenerate narrow bands. Therefore, the band structures of the open-shell TMOs (Fig. 6) show more concerning differences in how the different XC functionals describe the interatomic bonding. For example, BLYP describes the α and β electrons differently for CoO, as does B3LYP for CuO, as indicated by the dotted bands for β spin states. B3LYP tends to overestimate the magnitude of antiferromagnetic coupling, and thus fails at predicting magnetic properties of metals and semiconductors, which can be an explanation for the differences in the α and β bands for CuO. In addition, the fact that CoO and CuO have the strongest SOC and correlation effects may also contribute to this error.[133]

The electronic populations in TMO orbitals can be understood by looking at the DOS, which show a direct relation to the band dispersion, as illustrated in the atom-projected DOS calculated with selected XC functionals for CoO (Fig. 7) and CuO (Fig. 8). A high DOS at a specific energy level indicates that there are many states available for occupation. For CoO, the bands and DOS near E_F calculated with B3LYP, PBE0-1/3, HSE06 and HISS are very similar, with a predominance of TM states at the top of the valence bands (light blue line).

For CuO, the DOS of the valence bands for the GGA (within which E_F lies, corresponding to the zero band gap calculated) there is slightly more contribution from copper 3d orbitals (cyan). For mGGA M06L, with a narrow E_g of 0.37 eV, the copper 3d orbital states overlap with the oxygen 2p orbitals (pink line) at the valence band edge. For any XC approximation that

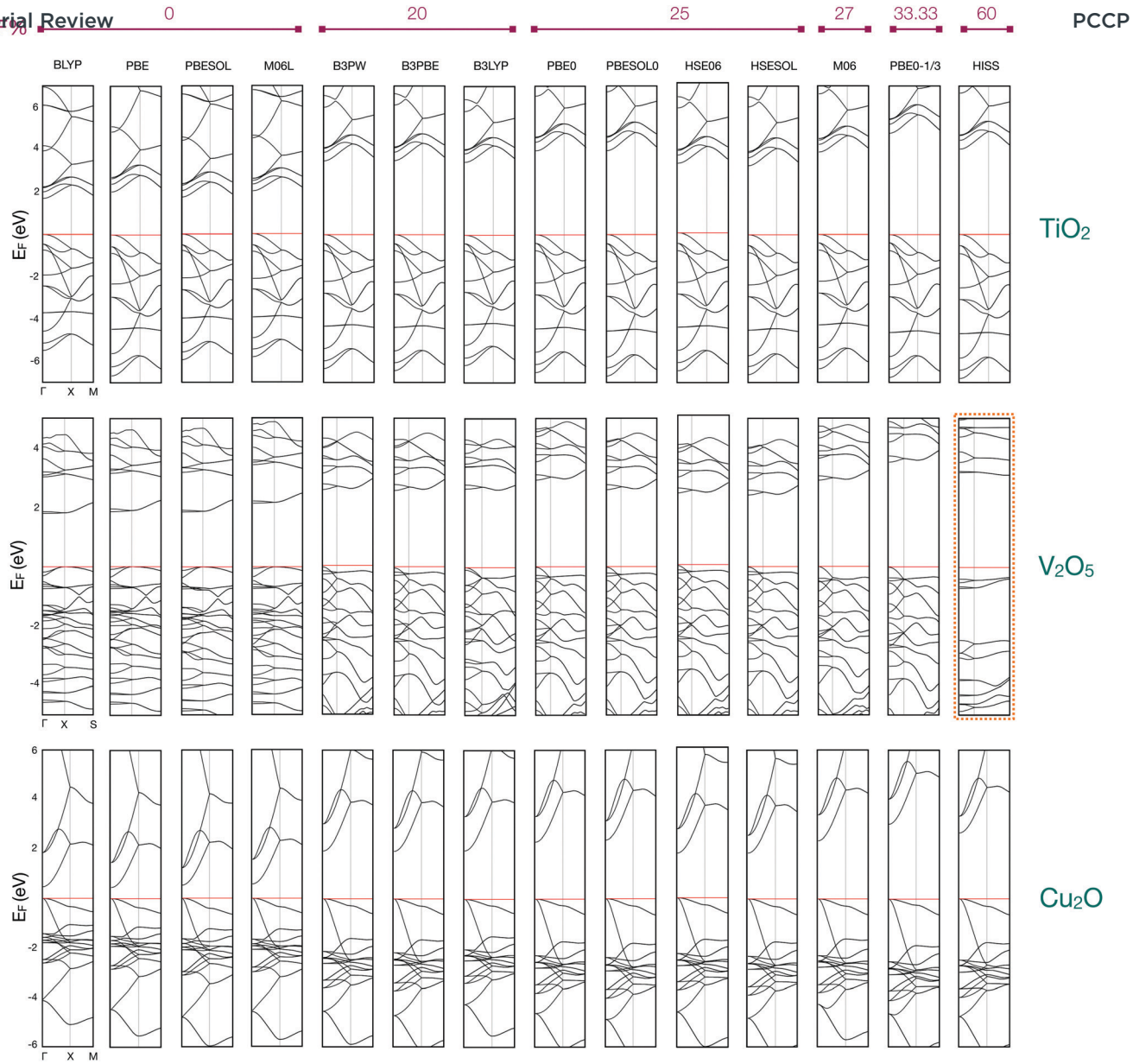

Fig. 5 Calculated band structures of selected closed-shell TMOs. The path of the Brillouin zone selected for investigation is shown in the first panel of each row. The Fermi level (E_F) was set to 0 eV and is indicated by the red line. The lines and numbers at the top indicate the amount of E_{HF} exchange for each density functional. The calculations for V_2O_5 include D3 corrections, except for the HISS DF (highlighted by the yellow box).

includes E_{HF}, namely B3LYP, PBE0-1/3, M06, HSE06, and HISS, the valence band edge is mainly dominated by oxygen 2p orbitals, which is a characteristic of p-type semiconductors.[134] This DOS predominance transition of TM 3d orbitals to 2p orbitals in the valence band maximum (VBM) upon addition of E_{HF} is also seen for Fe_2O_3 (Fig. S14, ESI†) and NiO (Fig. S16, ESI†), which are also p-type semiconductors.

In practice, band gaps, band structures and DOS are useful descriptors for many different materials and applications, such as for semiconductors to be used in photovoltaic or thermoelectric devices, or as catalysts, for which the desired properties can be tuned with band structure engineering techniques.[135–137] The effective mass of charge carriers can be obtained from the second derivative of the bands at high symmetry *k*-points at the VBM and conduction band minimum (CBM), and this provides information about the material's conductivity, for example. The 3d-band theory states that adsorption of molecules on heterogeneous catalyst surfaces occurs *via* electron transfer;[138] hence, based on an analysis of the band structure, DOS, and electronic conductivity we can learn about the electronic energies of occupied and available states for electron transfer, which is useful in the design of catalyst surfaces.[139,140]

We recommend that the choice of the XC functional for evaluating band gap and related properties be based firstly on the DF's theoretical formulation and grounding, rather than the degree of agreement with experimental results. The main rationale for this resides in four facts: (i) measured band gap values can vary significantly for a particular compound; (ii) some XC functionals result in good agreement with experimental values for the wrong reasons (*e.g.* cancellation of errors),

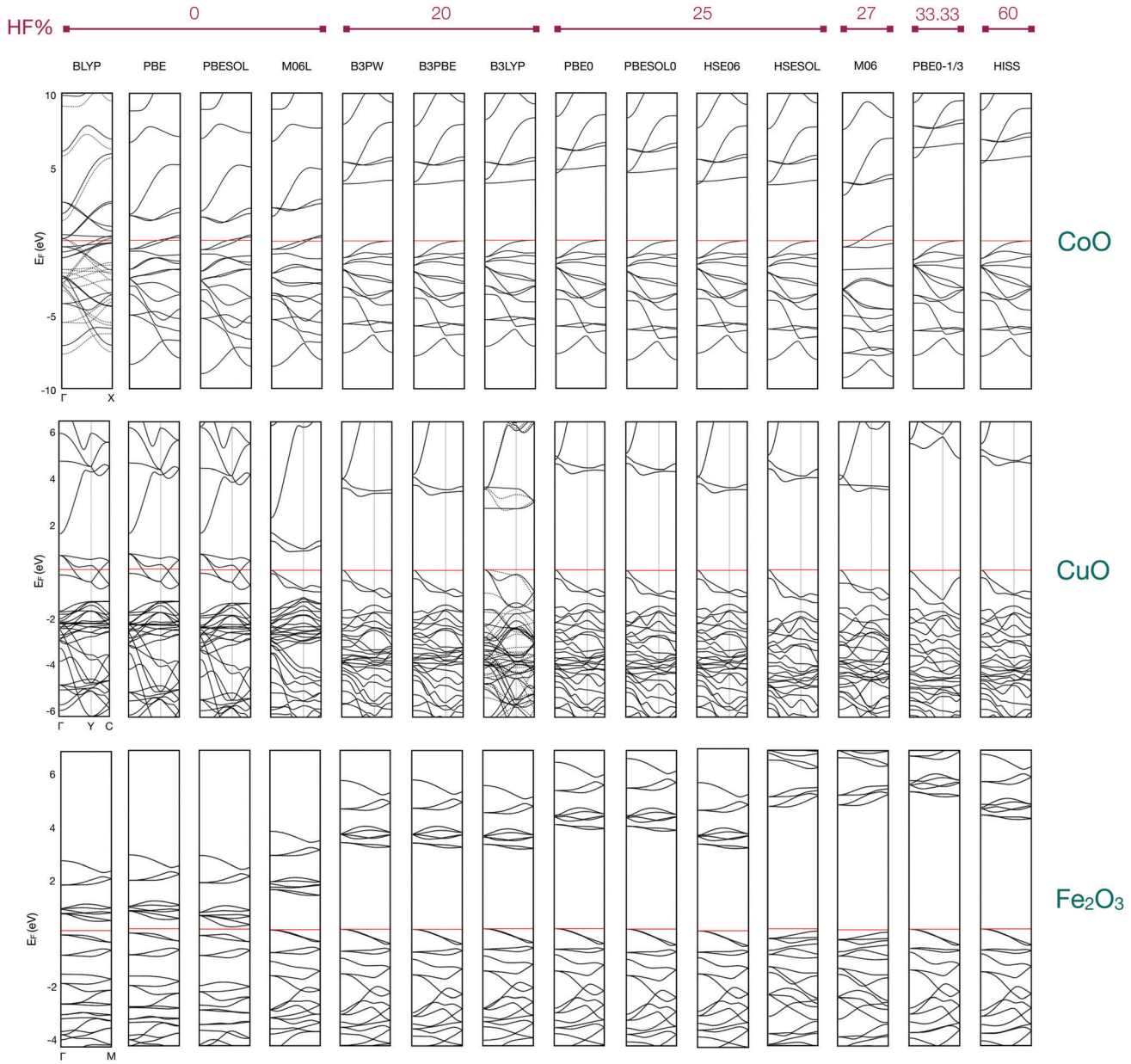

Fig. 6 Calculated band structures of selected open-shell TMOs. The path of the Brillouin zone selected for investigation is shown in the first panel of each row. The Fermi level (E_F) was set to 0 eV and is indicated by the red line. The lines and numbers at the top show the amount of E_{HF} exchange for each density functional.

as they lack a theoretical basis for their good performance; (iii) experimental E_g is determined as the difference between ionization potential and electron affinity (*e.g.* in UV-Vis spectroscopy), but the fundamental E_g^{DFT} calculated within the approximations of KS-DFT is the difference between the eigenvalues at the VBM and CBM, or between the lowest-unoccupied (LU) and highest-occupied (HO) one-electron energies from KS orbitals;[62,141] (iv) a good E_g predictions does not necessarily correspond to a correct description of the electronic structure of a TMO, because of the density dependency of the KS-DFT band gap, the well known DFT band gap problem (timeline in Fig. S1, ESI†).[142–146]

We encourage further reading on the challenges encountered in describing the antiferromagnetism in cubic 3d TMOs with DFT, which has stronger electromagnetic effects than in rutile or corundum TMOs, due to a 180° TM–O–TM interaction. Previous work on this interaction[147–149] has shown the difficulty of describing the broken symmetries of the electron density or spin density in DFT calculations of the strongly correlated electrons in 3d TMOs, and how this affects band-structure calculations, for example.

3.4 Magnetic moment (μ_B)

The colormap with δ_{approx} for the spin magnetic moments (μ_B) calculated with all XC functionals for the open-shell TMOs systems are provided in Fig. 9. The total magnetic moment experimental values with respective references, and calculated

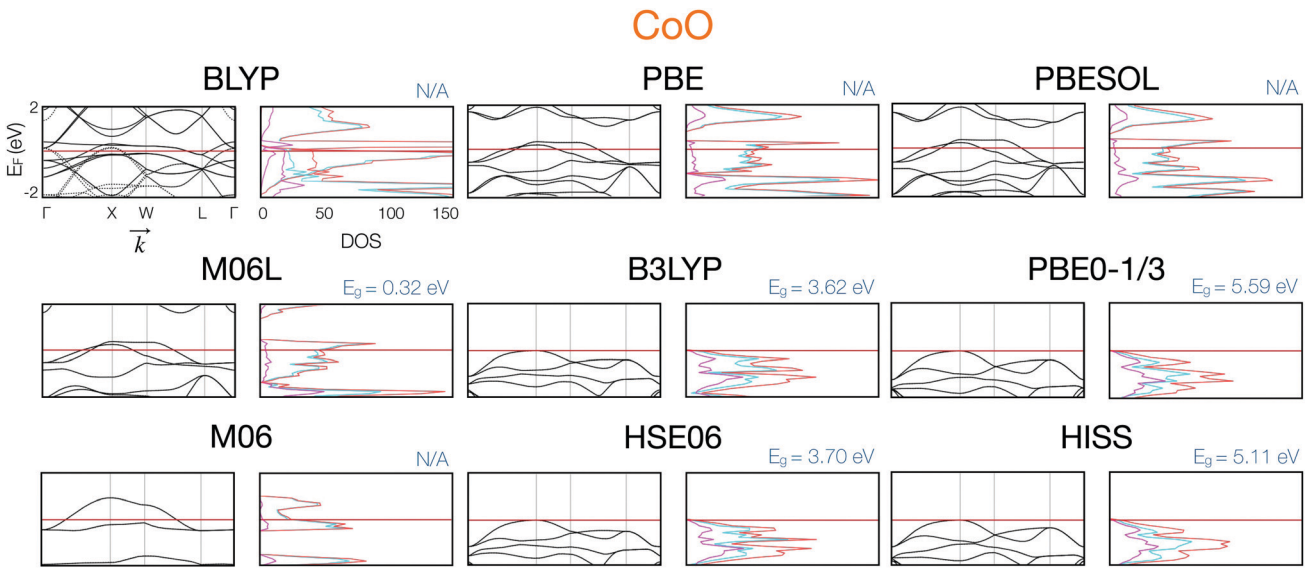

Fig. 7 Band structures and densities of states (DOS) of cubic monoxide CoO, calculated with various DFs. The Fermi level (E_F) was set to 0 eV and is indicated by the red line. The values at the right-hand top corner of the DOS for each DF are the calculated E_g. Color-code for DOS projections: red = total, cyan = cobalt, pink = oxygen.

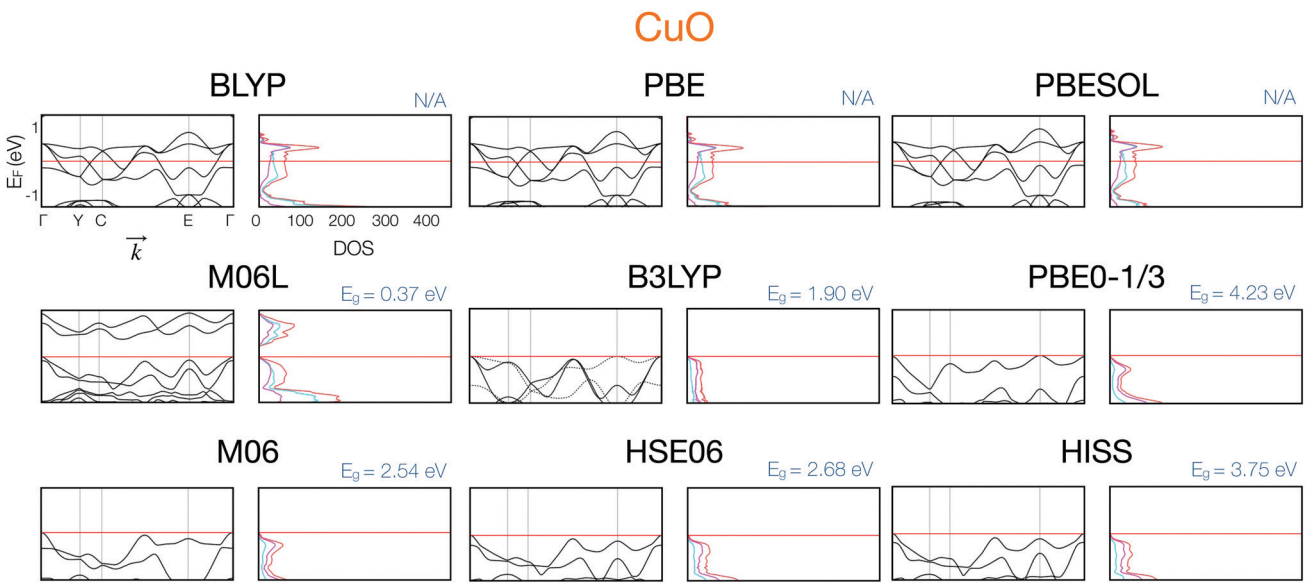

Fig. 8 Band structures and densities of states (DOS) of cubic monoxide CuO, calculated with various DFs. The Fermi level (E_F) was set to 0 eV and is indicated by the red line. The values at the right-hand top corner of the DOS for each DF are the calculated E_g. Color-code for DOS projections: red = total, cyan = copper, pink = oxygen.

μ_B values, are provided in Fig. S24 (ESI†). The calculated μ_B were obtained through Mulliken population analysis,[150] which reflects the spin and charge distribution of electrons across all atoms. The charge analysis and distribution is discussed in ESI† (Fig. S26–S28). The Mulliken population analysis is a popular orbital-dependent decomposition scheme, that derives spin and charge densities from deconstructing the electron occupations into atomic orbital and overlap populations.[151–155] Naturally, it follows that Mulliken population analysis is basis-dependent, which is significant in molecular systems because of the local nature of basis sets, but reduced in ionic systems, for which the basis set is optimized for crystal orbitals.[156–159] Since the calculated the TMOs μ_B with all DFs were compared using the same basis set, any error should be systematic.

Almost all XC functionals underestimate μ_B, indicated by the predominance of red shading in the colormap, although the magnitudes of underestimation vary. The only exceptions are CuO calculated with PBE0-1/3 and HISS. These two XC functionals have the highest values of E_{HF} (33.3% and 60%, respectively) and yield the best μ_B predictions for CuO, though

	GGA			mGGA	Global Hybrid						Hybrid mGGA	Range-Separated Hybrid			
TMO	BLYP	PBE	PBESOL	M06L	B3PW	B3PBE	B3LYP	PBE0	PBESOL0	PBE0-13	M06	HSE06	HSESOL	HISS	μ_B
CoO	31.04	33.51	35.59	28.91	24.68	24.83	24.80	23.93	24.75	22.90	27.83	24.08	24.82	22.95	3.58
CuO	N/A	N/A	N/A	25.96	10.85	10.32	12.12	4.93	6.35	-2.84	18.54	5.99	7.55	-0.68	0.67
Cr_2O_3	25.80	24.89	26.48	22.49	21.18	21.23	22.24	20.89	21.13	20.58	15.34	21.02	21.23	20.73	3.80
Fe_2O_3	20.12	19.44	25.33	11.57	8.04	7.94	8.85	6.81	7.19	5.28	7.72	7.06	7.38	5.33	4.64
MnO	8.74	8.03	9.17	7.86	4.57	4.73	5.34	4.29	4.74	3.90	3.31	4.34	4.72	3.65	5.00
NiO	23.16	23.86	28.47	12.34	7.79	8.07	7.47	5.82	7.66	3.32	10.50	6.21	7.86	3.76	1.77
V_2O_3	29.79	31.86	42.50	21.25	15.43	15.58	16.52	14.86	15.38	14.40	8.95	15.13	15.69	14.46	2.37
δ_{avg}	23.11	23.60	27.92	18.62	13.22	13.24	13.91	11.65	12.46	10.46	13.17	11.97	12.75	10.22	

Fig. 9 Relative approximation errors in spin magnetic moment (μ_B), color-coded by the relative difference from experimental values (right-hand column); average absolute errors δ_{avg} are given in the bottom row. N/A indicates XC functionals unable to describe μ_B for specific open-shell TMOs. References for experimental values are available in the ESI.†

slightly overestimated. For the other TMOs, PBE0-1/3 and HISS present the best performance for predicting μ_B with δ_{avg} of 10.46 and 10.22%, respectively. The only exceptions are for Cr_2O_3, MnO, and V_2O_5, for which the hybrid mGGA M06 (with the third highest value E_{HF}) gives the most accurate results when compared to PBE0-1/3 and HISS.

Towler *et al.* and other researchers observed that correlation effects tend to decrease μ_B, and SOC tend to increase μ_B by addition of the 3d orbital momenta contributions to the spin momenta.[153,160,161] Moreover, Randwanski and Ropka have shown, from first principles calculations, that the orbital magnetic moment for NiO and CoO AFMII monoxides are roughly 0.5 and 1.0μ_B, respectively.[162] The additional contribution of the orbital magnetic moment to the spin magnetic moment by adding SOC would correct the underestimated μ_B, especially in CoO and CuO, which have stronger spin–orbital and correlation interactions. Schrön *et al.* investigated the magnetic anisotropy in MnO, FeO, CoO, and NiO with the DFT + U approach.[163] In their study, relativistic effects were taken into account as mass corrections through the use of pseudopotentials and the inclusion of SOC. Their results for the absolute value of the total magnetic moments with both spin and orbital contributions for MnO, CoO, and NiO were 4.60, 2.93, and 1.79μ_B, respectively. Notably, MnO had no orbital momenta contribution according to Schrön, and previous experiments.[164] Interestingly, the values of μ_B with M06L are very similar for MnO (4.61μ_B), somewhat similar with PBE0-1/3 and HISS for NiO (1.71 and 1.70μ_B), and less similar for CoO (2.76 and 2.75μ_B) (Fig. S25, ESI†), respectively. The similarity of μ_B for NiO and CoO can be associated to the higher E_{HF} with PBE0-1/3 (33.3%) and HISS (60%), and the fact that def2-TZVP offers some benefits, even without relativistic corrections, when compared to effective-core potentials, which do include them.[165] Furthermore, Schrön obtained a lower than expected orbital moment contribution in CoO (0.25μ_B), and underestimation of $\sim$1μ_B to the experimental data, which was explained by a competing interplay between SOC, Coulomb repulsion, exchange and correlation effects. This competing interplay of quantum effects can be associated with higher underestimated values of μ_B in CoO, and it raises the question: why higher E_{HF} seem to reduce underestimation of μ_B—disregarding SOC—as noted by the lowest δ_{avg} values in PBE0-1/3 (10.46) and HISS (10.22)?

The trends in μ_B related to the amount of E_{HF} (Fig. S25, ESI†) show that a higher E_{HF} tends to increase the calculated μ_B. This is confirmed by the larger underestimation of μ_B for pure semi-local DFT, compared to the hybrids and RSH functionals. Interestingly, the introduction of short-range corrections to the E_{HF} exact exchange in the Hamiltonian in the RSH functionals does not seem to affect μ_B predictions, since HSE06 and HSESOL have similar δ_{approx} values when compared to the global hybrids with the same amount of E_{HF}, namely PBE0 and PBESOL0. In the case of HISS, which is a middle-range screened hybrid, lower δ_{approx} can be related to the higher E_{HF}%, as aforementioned. Additionally, the charge distribution in DFs with higher E_{HF}%, show how charges distribution tends towards a more ionic charter (Fig. S26–S28, ESI†). However, the best way to correct the underestimated μ_B is to account SOC by introducing relativistic effect corrections into the Hamiltonian to correctly assign orbital polarization.[166–170] Furthermore, higher E_{HF}% overestimates the E_g, hence showing how limited the DFs are in describing simultaneously electronic and magnetic properties.

We have discussed how the calculation of magnetic properties can show that different properties are strongly related to one another, *e.g.*, magnetic, electronic and geometric properties in 3d TMOs. The interplay between magnetic, structural,

and electronic properties is governed by charge, spin, crystal lattice, and orbital degrees of freedom, which gives rise to a variety of quantum effects that must be considered for a correct description of 3d electrons, and a reason why such electronic systems remain a theoretical challenge.[171] Understanding the intricate interplay of quantum effects in 3d TMOs is crucial to control structure–performance descriptors and properties such as quantic states in Fermi liquids, high-temperature superconductivity in cuprates, colossal magnetoresistance in manganites, charge density wave insulators (phasons an amplitudons), pseudo-gaps and polarons in superconductors for spintronics and electromagneto-optical applications.[172]

3.4.1 Spin contamination. The AFMII open-shell TMOs discussed in Section 3.4 have spin multiplicity ($2S_z + 1$) not equal to one, and therefore require the use of a broken symmetry approach to describe the α and β electrons, known as spin-polarized DFT or spin-unrestricted Kohn–Sham DFT (UKS). In UKS calculations, the spatial parts of the α and β electron spin–orbitals differ, resulting in the artificial mixing of spin states. This leads to a higher spin multiplicity than theoretical values, and is known as spin contamination (SC).[71,72,173] As a consequence of SC, the UKS determinants can no longer be considered eigenfunctions of the total spin $\hat{S}^2$ operator:

$$\langle \hat{S}^2 \rangle = S_z(S_z + 1) \quad (3)$$

Fig. S29 (ESI†) provides a colormap of the values for $\langle \hat{S}^2 \rangle_{\mathrm{UKS}}$ for all the spin-polarized TMOs. In most cases, the presence of SC affects mostly the structural parameters (ρ_{bulk}) and spin populations (μ_{B}), as discussed in Sections 3.1 and 3.4, and in the literature.[31,71,72,173]

Some authors claim that open-shell systems treated with UKS DFT are less prone to SC when compared to wave-function methods, because electron correlation is included in the single-determinant wave function.[31] Other authors have claimed that the proper definition of SC in DFT lacks rigor.[174–176] In fact, most discussions about SC are based on wave function methods, evaluating highly delocalized molecular radicals, in which SC is prominent.[177,178] Schattenberg and coworkers revisited a benchmark of DFs to describe hyperfine coupling in open-shell 3d TM centers, highlighting the need to address SC in the development of implemented DFs.[179] In a recent study, Dovesi and coworkers studied superexchange interactions in TM compounds, and found that spin density and the energetics of the various spin states can be reasonably accurate in periodic TM systems, in contrast to TM molecular complexes.[72] The authors explain that besides the greater importance of electron correlation in the latter TM molecular complexes, spin-polarized periodic systems benefits from: (i) energy differences between spin states due to ionic bonding character; (ii) reduced number of possible states due to high symmetry. As observed in previous studies,[71,179] the degree SC depends on the spin state (high or low), as well as the level-of-theory and method, but more investigations are necessary to shed light on the topic.[180]

3.5 High frequency linear optical properties

High frequency linear optical dielectric constants (ε_∞), and refractive indices (n) of the TMOs were calculated through the Coupled Perturbed Kohn–Sham (CPKS) method,[107–109] and compared to the experimental values (Fig. 10 and 11). The CPKS scheme allows analytical computation of the linear and nonlinear optical properties self-consistently, by introducing a perturbative static electric field to the Hamiltonian. The optical properties are obtained through the second derivative of the perturbed energy, which is the polarizability (α) second-rank tensor, analytically evaluated in all directions; from this, the dielectric tensor (ε), and dielectric susceptibility (χ) can be obtained. The refractive index is related to the eigenvalues of the principal axis of the dielectric tensor, and can be obtained by eqn (4), as defined by Maxwell:[181]

$$n_i = \sqrt{\varepsilon_i} \quad \text{with} \quad i = 1, 2, 3 \quad (4)$$

The average of the diagonalized matrix principal axes gives the calculated values of ε_∞ and n, which can be compared to experimental values, as presented in Fig. S30 and S31 (ESI†). Comparison of experimental ε_∞ of the anisotropic TMOs was done in specific directions, namely CuO ($\parallel$ b axis), Cr_2O_3 ($\parallel$ c axis), and ZnO ($\parallel$ c axis). The CPKS availability for different XC functionals is limited, which is why results are only shown for a smaller selection of functionals than for properties presented earlier.

By definition, α depends on the density matrix and is inversely proportional to the KS energy gap E_g obtained in the CPKS scheme.[109] Therefore, a well defined band structure, as discussed in detail earlier, is a prerequisite to obtaining accurate ε_∞ and consequently n. In fact, this is what we see in the colormap (Fig. 10), *i.e.*, δ_{avg} improves ~34% going from all GGA to the global hybrids DFs with the lowest δ_{avg}. Dark colors indicating significant overestimations (dark blue) and underestimations (dark red) in ε_∞ predictions with the GGA functionals occurs notably for some open-shell systems, *e.g.*, CoO, CuO, Cr_2O_3, Fe_2O_3, MnO, and NiO. For these TMOs, δ_{approx} magnitude is significantly higher compared to the closed-shell systems Cu_2O, ZnO, and TiO_2. The erratic behavior in δ_{approx} for the open-shell TMOs is a result of the energy convergence to a conducting state with the GGA functionals through the perturbed Hamiltonian of the CPKS scheme, in contrast to the observed conductors CoO and CuO in the band structure analysis.

The results obtained with the hybrid DFs show that the amount of E_{HF} seems to have little effect on ε_∞ predictions. This can be seen by comparing δ_{avg} of DFs with 20% E_{HF}, namely B3PW, B3PBE and B3LYP, to PBE0, PBESOL0 with 25% E_{HF}, and PBE0-1/3, with 33.3% E_{HF}, showing that δ_{avg} changes about 13%. Across all the XC functionals, the lowest δ_{avg} values (below 15% of δ_{avg}) are in the order: B3PBE < B3PW < B3LYP.

The ε_∞ is a property that reflects the electric permittivity of insulating materials, related to their ability to store energy in an electrical field. The index of refraction determines the speed of

	GGA			Global Hybrid						
TMOs	PBE	BLYP	PBESOL	B3PW	B3PBE	B3LYP	PBE0	PBESOL0	PBE0-13	ε_∞
CoO	58.23	37.66	-43.87	9.22	8.69	10.03	16.75	14.87	25.15	5.30
CuO	58.92	61.26	79.28	15.01	14.42	18.38	22.89	20.87	32.35	5.90
Cu_2O	-28.26	-16.14	-31.87	10.18	8.07	14.60	14.16	13.29	21.99	6.46
Cr_2O_3	-64.31	-63.23	81.92	7.25	6.99	8.56	13.04	11.63	20.34	5.97
Fe_2O_3	61.61	46.86	57.08	18.65	18.91	18.21	26.26	25.48	34.63	6.70
MnO	-50.02	-53.94	-56.46	11.64	10.84	12.67	16.28	15.13	22.72	4.95
NiO	69.77	69.28	62.03	9.74	9.48	10.10	19.16	16.77	28.86	5.70
ZnO	-15.25	-9.72	-20.18	10.11	9.10	11.61	12.68	11.50	17.05	3.75
TiO_2	-6.75	-6.15	-8.09	4.71	4.68	5.29	9.73	14.02	16.66	7.37
δ_{avg}	40.47	45.90	48.98	10.72	10.13	12.16	16.77	15.95	24.42	

Over
Under

Fig. 10 Relative approximation errors in high frequency dielectric constant (ε_∞), color-coded by the relative difference from experimental values (right-hand column); average absolute errors δ_{avg} are given in the bottom row. References for experimental values are available in the ESI.†

	GGA			Global Hybrid						
TMOs	PBE	BLYP	PBESOL	B3PW	B3PBE	B3LYP	PBE0	PBESOL0	PBE0-13	n
CuO	-15.21	-90.46	-33.64	8.79	8.67	9.75	14.60	13.30	20.89	2.63
Cu_2O	-1.35	3.55	-2.77	15.18	14.19	17.30	17.08	16.66	20.96	2.84
Fe_2O_3	-108.75	-151.21	-119.66	13.92	14.15	13.27	18.79	18.31	24.30	2.91
MnO	-26.16	-27.79	-28.84	3.18	2.74	3.74	5.75	5.29	9.45	2.16
NiO	-75.13	-76.56	-96.30	4.30	4.16	4.49	9.43	8.10	15.03	2.37
V_2O_3	-23.35	13.47	-76.07	0.76	11.75	13.47	17.04	15.82	22.21	2.80
ZnO	-3.57	-0.92	-6.01	9.36	8.87	10.03	10.68	10.09	12.93	2.01
TiO_2	-7.38	-7.08	-8.05	4.97	4.95	5.27	7.41	7.06	10.89	2.61
δ_{avg}	46.38	32.61	46.42	7.56	8.68	9.67	12.60	11.83	17.08	

Over
Under

Fig. 11 Relative approximation errors in refractive index (n), color-coded by the relative difference from experimental values (right-hand column); average absolute errors δ_{avg} are given in the bottom row. References for experimental values are available in the ESI.†

light passing through materials and can be used to develop optical instruments. Therefore, it is essential to accurately predict ε_∞ and n, as both optical properties can be tailored to produce materials for technological applications such as capacitors,[182] nanophotonic devices,[183] microelectronic devices, *e.g.*, central processing units (CPU), dynamic random-access memory (DRAM) and flash memory,[184] high power electronic devices and solar-blind ultraviolet (UV) photodetectors.[185]

3.6 Overall performance and concluding remarks

The overall performances of the DFs for the properties of TMOs, in addition to the average computational cost in seconds per SCF cycle (t/SCF), are depicted in the spider plots shown in Fig. 12. The properties on the axes of each plot are represented as a normalized δ_{avg} value, ranging from 0 to 1, obtained by dividing δ_{avg} for each DF by the highest δ_{avg} obtained for that property across all DFs. The δ_{avg} colormap (Fig. S32, ESI†), and separate spider plots for each DF (Fig. S33), are available in the ESI.† Accordingly, DFs with the largest colored areas have the highest deviation in calculated properties from experimental values, and the DFs with the smallest colored areas have the least deviation. Similarly, scores near 1 for computational cost represent the most expensive choices of DFs. The optical properties ε_∞ and n do not appear for M06L, M06, HSE06, HSESOL, and HISS, because the CPKS scheme is not available for these DFs (M06L* and grey area in Fig. 12(c)).

We recommend the ρ_{bulk} (3rd axis clock-wise) as the first property for choosing a DF, because of the standardized experimental data available from X-ray crystallographic structures, and also because the ρ_{bulk} can be directly related to the experimental value. Secondly, the ω_v (4th axis), has great reliability and abundance of experimental IR and Raman data, direct physical interpretation of vibrational frequency when compared to calculated data, and allows to evaluate the ground-state structure obtained (absence of imaginary frequencies). After that, we recommend the band gap (1st axis), with appropriate analysis of the band structure and DOS. The electronic properties are critical when it comes to the choice of DFs, since this is where GGA fails the most. The μ_B (2nd axis clock-wise) of TMOs with unrestricted spin configurations come next, mainly because the calculated values are considerably affected by the absence of relativistic corrections. The optical properties ε_∞ and n (5th and 6th axes) reflect the values obtained for band gap, but since in our analysis the CPKS method was limited to a number of DFs, further dedicated studies are necessary. The computational cost (7th axis), is a major bottleneck for highly-accurate DFT calculations for periodic systems. For realistic models, it is not uncommon to require supercells with a large number of atoms (>200), which makes RSH functionals prohibitive, as they are very costly ($10 \times t$/SCF compared with the GGA functionals). The mGGA M06L deserves highlighting for its significant overall better performance compared to GGA, at no increase of computational resources, as does the hybrid mGGA M06 when compared to global hybrids. Since we have only analyzed M06L and M06 for these types of XC functionals, further investigation would be necessary to reach conclusions on their overall performance.

With currently available computational resources, it is increasingly feasible to employ global hybrids rather than the most used GGA functionals, even though they are approximately five times more computationally demanding. The benefits of employing global hybrids for the electronic properties of TMOs, *e.g.*, band structure and DOS, are the better estimation of KS orbitals energy levels, hence band gap prediction. For this reason, in situations where electronic properties are being evaluated and tailored, global hybrids are worth the extra cost.

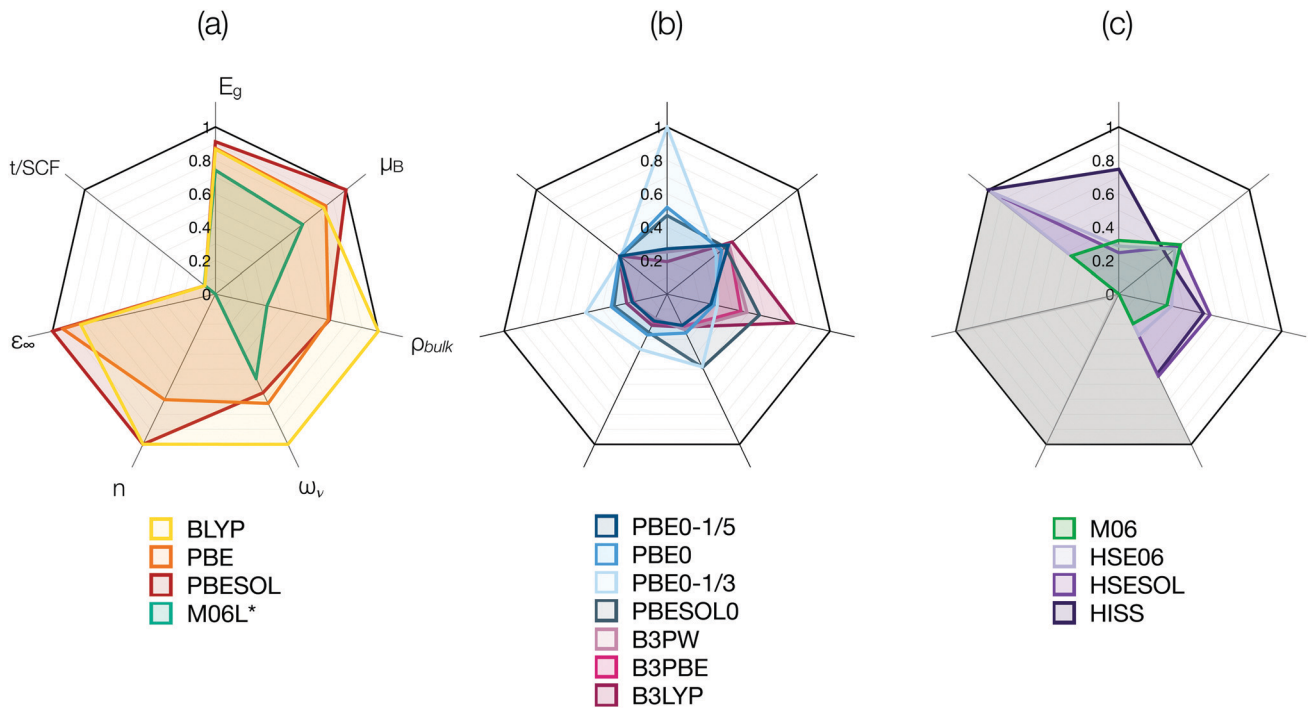

Fig. 12 Spider plots of normalized average of absolute approximation error (δ_{avg}) for band gap (E_g), magnetic moment (μ_B), bulk density (ρ_{bulk}), vibrational frequency (ω_v), refractive index (n), dielectric constant (ε_∞), and computational cost (t/SCF): (a) GGA and mGGA, (b) global hybrids, and (c) hybrid mGGA and RSH. The M06L* and grey area in (c) represent the absence of CPKS results.

Comparing all DFs, the best predictions for ρ_{bulk} and ω_v come from PBE0, but this is not the case for E_g, for which the most accurate results are obtained with the 20% E_{HF} functionals of the B3 family. For this reason, we have included PBE0-1/5 in Fig. 12(b), to confirm that changing E_{HF} from 25% to 20% in PBE0 can improve E_g without compromising the accuracy in the other properties. In fact, PBE0-1/5 not only significantly corrects E_g, but also ρ_{bulk} and ω_v; the only property not improved is μ_B, which worsens by 1.47%. With PBE0-1/5, δ_{avg} of E_g (19.67%) becomes, comparable to B3PW (18.29%) and B3PBE (18.85%), but δ_{avg} for ρ_{bulk} and ω_v are better with PBE0-1/5 (Fig. S29, ESI†). Based on these results, we show that choosing a hybrid XC functional to use in design and evaluation of 3d TMOs, including studying the electronic properties, should made with careful consideration. Hence, further investigation on TMOs properties, considering SOC, is necessary to verify why PBE0-1/5 is optimal, since we do not analyse its theoretical grounding, but we observe that it improved predictions of ρ_{bulk} and ω_v, and E_g when compared to the best DFs B3PW, B3PBE, and B3LYP.

Future DF benchmark studies of 3d TMOs should aim to evaluate properties such as exchange coupling and/or Néel temperature since they are more sensitive to the DFT self-interaction error. Moreover, the interplay of quantum effects including spin, charge, lattice and orbital degrees of freedom should be explored. This could include discussion of the effect of exchange on some observables, *e.g.*, magnetic coupling or order of levels in the band structure, but should be expanded to understand the behavior of DFs for designing materials for relevant fields, such as current energy applications. The critical point to develop optimized DFs for materials design modelling is to understand the effect of DFs on various calculated properties so that one can make an optimal informed choice depending on the chemical problem being addressed, and to aid the development of new DFs suitable for periodic systems.

Data availability

The data that supports the findings of this study are available within the article and its ESI.† It includes a summary of theoretical background, information on the crystallographic structures, spin configuration of open-shell TMOs, calculated data for all properties, band structures and DOS plots for all DFs, experimental references, geometry optimization inputs and basis sets.

Author contributions

I. Ø. conceptualized the research framework, performed the calculations, investigation and visualization, and wrote the original draft of the manuscript. I. Ø., P. B., J. N. H. carried out the formal analysis. A. H., P. B. and B. H. provided resources and supervision. All authors discussed the results and contributed to reviewing and editing of the manuscript.

Conflicts of interest

The authors declare no conflict of interests.

Acknowledgements

I. Ø. thanks University of New South Wales (UNSW) for a Scientia PhD Scholarship. This research was undertaken with the assistance of resources and services from the National Computational Infrastructure, which is supported by the Australian Government through the UNSW-NCI partner scheme; the Multi-modal Australian ScienceS Imaging and Visualisation Environment (MASSIVE); the Pawsey Supercomputing Centre, which is supported by the Australian Government and the Government of Western Australia; and was enabled by Intersect Australia Limited. Part of this work was funded by ARENA as part of ARENA's Research and Development Program-Solar PV Research (Grant No. 2017/RND007). The authors also thank G. Caramori and F. Corà for the incentive, and Lorenzo Maschio, Silvia Casassa, Jacques Desmarais, and Mohammed Al-Farsi for the support and advice.

Notes and references

1 C. N.-R. Rao, *Annu. Rev. Phys. Chem.*, 1989, **40**, 291–326.
2 K. Kar, *Handbook of nanocomposite supercapacitor materials. Characteristics*, Springer International Publishing AG, Cham, 2020.
3 A. A.-S. Devi and D. Murali, *Chemically Deposited Nanocrystalline Metal Oxide Thin Films*, Springer International Publishing, 2021, pp. 85–97.
4 A. Moulson, *Concise Encyclopedia of Advanced Ceramic Materials*, Elsevier, 1991, pp. 497–499.
5 P. A. Cox, *Transition metal oxides: an introduction to their electronic structure and properties*, Clarendon Press Oxford University Press, Oxford New York, 2010.
6 M. D. Bhatt and J. Y. Lee, *Energy Fuels*, 2020, **34**, 6634–6695.
7 M. Song, Y. Song, W. Sha, B. Xu, J. Guo and Y. Wu, *Catalysts*, 2020, **10**, 141.
8 C. Yuan, H. B. Wu, Y. Xie and X. W.-D. Lou, *Angew. Chem., Int. Ed.*, 2014, **53**, 1488–1504.
9 W. T. Hong, M. Risch, K. A. Stoerzinger, A. Grimaud, J. Suntivich and Y. Shao-Horn, *Energy Environ. Sci.*, 2015, **8**, 1404–1427.
10 F. Song, L. Bai, A. Moysiadou, S. Lee, C. Hu, L. Liardet and X. Hu, *J. Am. Chem. Soc.*, 2018, **140**, 7748–7759.
11 M. Beller, *Chem. Rev.*, 2019, **119**, 2089.
12 K. D. Vogiatzis, M. V. Polynski, J. K. Kirkland, J. Townsend, A. Hashemi, C. Liu and E. A. Pidko, *Chem. Rev.*, 2018, **119**, 2453–2523.
13 A. Nandy, C. Duan, M. G. Taylor, F. Liu, A. H. Steeves and H. J. Kulik, *Chem. Rev.*, 2021, **121**, 9927–10000.
14 J. Linnera, G. Sansone, L. Maschio and A. J. Karttunen, *J. Phys. Chem. C*, 2018, **122**, 15180–15189.
15 W. Li, J. Shi, K. H.-L. Zhang and J. L. MacManus-Driscoll, *Mater. Horiz.*, 2020, **7**, 2832–2859.

16 Y. Wang, H. Su, Y. He, L. Li, S. Zhu, H. Shen, P. Xie, X. Fu, G. Zhou, C. Feng, D. Zhao, F. Xiao, X. Zhu, Y. Zeng, M. Shao, S. Chen, G. Wu, J. Zeng and C. Wang, *Chem. Rev.*, 2020, **120**, 12217–12314.
17 M. Wang, H. Yang, J. Shi, Y. Chen, Y. Zhou, L. Wang, S. Di, X. Zhao, J. Zhong, T. Cheng, W. Zhou and Y. Li, *Angew. Chem., Int. Ed.*, 2021, **60**, 5771–5777.
18 P. Nuss and M. J. Eckelman, *PLoS One*, 2014, **9**, e101298.
19 P. C.-K. Vesborg and T. F. Jaramillo, *RSC Adv.*, 2012, **2**, 7933.
20 P. Parida, R. Kashikar, A. Jena and B. Nanda, *J. Phys. Chem. Sol.*, 2018, **123**, 133–149.
21 W. L. Roth, *Phys. Rev.*, 1958, **110**, 1333–1341.
22 Y. Tokura and N. Nagaosa, *Science*, 2000, **288**, 462–468.
23 F. Corà, M. Alfredsson, G. Mallia, D. S. Middlemiss, W. C. Mackrodt, R. Dovesi and R. Orlando, *The Performance of Hybrid Density Functionals in Solid State Chemistry*, Springer Berlin Heidelberg, Berlin, Heidelberg, 2004, pp. 171–232.
24 R. Zimmermann, P. Steiner, R. Claessen, F. Reinert, S. Hüfner, P. Blaha and P. Dufek, *J. Phys: Condens. Matter*, 1999, **11**, 1657–1682.
25 Z.-J. Zhao, S. Liu, S. Zha, D. Cheng, F. Studt, G. Henkelman and J. Gong, *Nat. Rev. Mater.*, 2019, **4**, 792–804.
26 S. Sinthika, U. V. Waghmare and R. Thapa, *Small*, 2017, **14**, 1703609.
27 P. Hohenberg and W. Kohn, *Phys. Rev.*, 1964, **136**, B864–B871.
28 W. Kohn and L. J. Sham, *Phys. Rev.*, 1965, **140**, A1133–A1138.
29 J. Neugebauer and T. Hickel, *Wiley Interdiscip. Rev.: Comput. Mol. Sci.*, 2013, **3**, 438–448.
30 F. M. Bickelhaupt and E. J. Baerends, in *Rev. Comput. Chem.*, ed. K. B. Lipkowitz and D. B. Boyd, Wiley, New York, 2000, **15**, pp. 1–86.
31 F. Jensen, *Introduction to Computational Chemistry*, John Wiley & Sons, Incorporated, Somerset, 2016.
32 W. Koch and M. C. Holthausen, *A Chemist's Guide to Density Functional Theory*, Wiley, 2001.
33 N. Marzari, A. Ferretti and C. Wolverton, *Nat. Mater.*, 2021, **20**, 736–749.
34 S. G. Louie, Y.-H. Chan, F. H. da Jornada, Z. Li and D. Y. Qiu, *Nat. Mater.*, 2021, **20**, 728–735.
35 J. E. Saal, S. Kirklin, M. Aykol, B. Meredig and C. Wolverton, *J. Mater.*, 2013, **65**, 1501–1509.
36 A. Jain, G. Hautier, C. J. Moore, S. P. Ong, C. C. Fischer, T. Mueller, K. A. Persson and G. Ceder, *Comput. Mater. Sci.*, 2011, **50**, 2295–2310.
37 D. D. Landis, J. S. Hummelshoj, S. Nestorov, J. Greeley, M. Dulak, T. Bligaard, J. K. Nørskov and K. W. Jacobsen, *Comput. Sci. Eng.*, 2012, **14**, 51–57.
38 S. Curtarolo, W. Setyawan, S. Wang, J. Xue, K. Yang, R. H. Taylor, L. J. Nelson, G. L. Hart, S. Sanvito, M. Buongiorno-Nardelli, N. Mingo and O. Levy, *Comput. Mater. Sci.*, 2012, **58**, 227–235.
39 S. Kim, M. Lee, C. Hong, Y. Yoon, H. An, D. Lee, W. Jeong, D. Yoo, Y. Kang, Y. Youn and S. Han, *Sci. Data*, 2020, **7**, 387.
40 M. Kuklin, K. Eklund, J. Linnera, A. Ropponen, N. Tolvanen and A. Karttunen, *Molecules*, 2022, **27**, 874.
41 C. Adamo and V. Barone, *J. Chem. Phys.*, 1999, **110**, 6158–6170.
42 S. H. Vosko, L. Wilk and M. Nusair, *Can. J. Phys.*, 1980, **58**, 1200–1211.
43 J. P. Perdew, *AIP Conf. Proc.*, 2001, **577**, 1–20.
44 F. Weigend and R. Ahlrichs, *Phys. Chem. Chem. Phys.*, 2005, **7**, 3297.
45 A. D. Becke, *J. Chem. Phys.*, 2014, **140**, 18A301.
46 P. Morgante and R. Peverati, *J. Quantum Chem.*, 2020, **120**(18), e26332.
47 H. S. Yu, S. L. Li and D. G. Truhlar, *J. Chem. Phys.*, 2016, **145**, 130901.
48 S. Hammes-Schiffer, *Science*, 2017, **355**, 28–29.
49 M. G. Medvedev, I. S. Bushmarinov, J. Sun, J. P. Perdew and K. A. Lyssenko, *Science*, 2017, **355**, 49–52.
50 M. G. Medvedev, I. S. Bushmarinov, J. Sun, J. P. Perdew and K. A. Lyssenko, *Science*, 2017, **356**, 496.
51 K. P. Kepp, *Science*, 2017, **356**, 496.
52 C. J. Cramer and D. G. Truhlar, *Phys. Chem. Chem. Phys.*, 2009, **11**, 10757.
53 W. Li, C. F.-J. Walther, A. Kuc and T. Heine, *J. Chem. Theory Comput.*, 2013, **9**, 2950–2958.
54 V. L. Chevrier, S. P. Ong, R. Armiento, M. K.-Y. Chan and G. Ceder, *Phys. Rev. B: Condens. Matter Mater. Phys.*, 2010, **82**(7), 075122.
55 P. Borlido, J. Schmidt, A. W. Huran, F. Tran, M. A.-L. Marques and S. Botti, *Npj Comput. Mater.*, 2020, **6**(96), 1–17.
56 K. Sharkas, K. Wagle, B. Santra, S. Akter, R. R. Zope, T. Baruah, K. A. Jackson, J. P. Perdew and J. E. Peralta, *Proc. Natl. Acad. Sci. U. S. A.*, 2020, **117**, 11283–11288.
57 Q. Zhao and H. J. Kulik, *J. Phys. Chem. Lett.*, 2019, **10**, 5090–5098.
58 D. Hait and M. Head-Gordon, *J. Phys. Chem. Lett.*, 2018, **9**, 6280–6288.
59 J. L. Bao, L. Gagliardi and D. G. Truhlar, *J. Phys. Chem. Lett.*, 2018, **9**, 2353–2358.
60 F. Liu and H. J. Kulik, *J. Chem. Theory Comput.*, 2019, **16**, 264–277.
61 J. Tao, J. P. Perdew, V. N. Staroverov and G. E. Scuseria, *Phys. Rev. Lett.*, 2003, **91**(14), 146401.
62 J. P. Perdew, W. Yang, K. Burke, Z. Yang, E. K.-U. Gross, M. Scheffler, G. E. Scuseria, T. M. Henderson, I. Y. Zhang, A. Ruzsinszky, H. Peng, J. Sun, E. Trushin and A. Görling, *Proc. Natl. Acad. Sci. U. S. A.*, 2017, **114**, 2801–2806.
63 P. Kratzer and J. Neugebauer, *Front. Chem.*, 2019, **7**, 1–18.
64 M. Valiev, E. J. Bylaska and J. H. Weare, *J. Chem. Phys.*, 2003, **119**, 5955–5964.
65 P. Calaminici, F. Janetzko, A. M. Köster, R. Mejia-Olvera and B. Zuniga-Gutierrez, *J. Chem. Phys.*, 2007, **126**, 044108.
66 K. Adhikari, A. Chakrabarty, O. Bouhali, N. Mousseau, C. S. Becquart and F. El-Mellouhi, *J. Comput. Sci.*, 2018, **29**, 163–167.
67 K. Lejaeghere, V. V. Speybroeck, G. V. Oost and S. Cottenier, *Crit. Rev. Solid State Mater. Sci.*, 2013, **39**, 1–24.

68 K. Lejaeghere, G. Bihlmayer, T. Björkman, P. Blaha, S. Blügel, V. Blum, D. Caliste, I. E. Castelli, S. J. Clark, A. D. Corso, S. de Gironcoli, T. Deutsch, J. K. Dewhurst, I. D. Marco, C. Draxl, M. Dułak, O. Eriksson, J. A. Flores-Livas, K. F. Garrity, L. Genovese, P. Giannozzi, M. Giantomassi, S. Goedecker, X. Gonze, O. Grånäs, E. K.-U. Gross, A. Gulans, F. Gygi, D. R. Hamann, P. J. Hasnip, N. A.-W. Holzwarth, D. Iusan, D. B. Jochym, F. Jollet, D. Jones, G. Kresse, K. Koepernik, E. Küçükbenli, Y. O. Kvashnin, I. L.-M. Locht, S. Lubeck, M. Marsman, N. Marzari, U. Nitzsche, L. Nordström, T. Ozaki, L. Paulatto, C. J. Pickard, W. Poelmans, M. I.-J. Probert, K. Refson, M. Richter, G.-M. Rignanese, S. Saha, M. Scheffler, M. Schlipf, K. Schwarz, S. Sharma, F. Tavazza, P. Thunström, A. Tkatchenko, M. Torrent, D. Vanderbilt, M. J. van Setten, V. V. Speybroeck, J. M. Wills, J. R. Yates, G.-X. Zhang and S. Cottenier, *Science*, 2016, **351**(6280), aad3000.
69 A. J. Cohen, P. Mori-Sánchez and W. Yang, *Chem. Rev.*, 2011, **112**, 289–320.
70 R. Dovesi, R. Orlando, A. Erba, C. M. Zicovich-Wilson, B. Civalleri, S. Casassa, L. Maschio, M. Ferrabone, M. D.-L. Pierre, P. DArco, Y. Noël, M. Causà, M. Rérat and B. Kirtman, *Int. J. Quantum Chem.*, 2014, **114**, 1287–1317.
71 R. Dovesi, A. Erba, R. Orlando, C. M. Zicovich-Wilson, B. Civalleri, L. Maschio, M. Rérat, S. Casassa, J. Baima, S. Salustro and B. Kirtman, *Wiley Interdiscip. Rev.: Comput. Mol. Sci.*, 2018, **8**(4), e1360.
72 R. Dovesi, F. Pascale, B. Civalleri, K. Doll, N. M. Harrison, I. Bush, P. D'Arco, Y. Noël, M. Rérat, P. Carbonnière, M. Causà, S. Salustro, V. Lacivita, B. Kirtman, A. M. Ferrari, F. S. Gentile, J. Baima, M. Ferrero, R. Demichelis and M. D.-L. Pierre, *J. Chem. Phys.*, 2020, **152**, 204111.
73 J. K. Desmarais, A. Erba, J.-P. Flament and B. Kirtman, *J. Chem. Theory Comput.*, 2021, **17**, 4712–4732.
74 J. P. Perdew, A. Ruzsinszky, J. Tao, V. N. Staroverov, G. E. Scuseria and G. I. Csonka, *J. Chem. Phys.*, 2005, **123**, 062201.
75 J. P. Perdew, K. Burke and M. Ernzerhof, *Phys. Rev. Lett.*, 1996, **77**, 3865–3868.
76 J. P. Perdew, A. Ruzsinszky, G. I. Csonka, O. A. Vydrov, G. E. Scuseria, L. A. Constantin, X. Zhou and K. Burke, *Phys. Rev. Lett.*, 2008, **100**(13), 136406.
77 A. D. Becke, *Phys. Rev. A: At., Mol., Opt. Phys.*, 1988, **38**, 3098–3100.
78 C. Lee, W. Yang and R. G. Parr, *Phys. Rev. B: Condens. Matter Mater. Phys.*, 1988, **37**, 785–789.
79 Y. Zhao and D. G. Truhlar, *J. Chem. Phys.*, 2006, **125**, 194101.
80 A. D. Becke, *J. Chem. Phys.*, 1993, **98**, 5648–5652.
81 J. P. Perdew and Y. Wang, *Phys. Rev. B: Condens. Matter Mater. Phys.*, 1992, **45**, 13244–13249.
82 C. A. Guido, E. Brémond, C. Adamo and P. Cortona, *J. Chem. Phys.*, 2013, **138**, 021104.
83 Y. Zhao and D. G. Truhlar, *Theor. Chem. Acc.*, 2007, **120**, 215–241.
84 A. V. Krukau, O. A. Vydrov, A. F. Izmaylov and G. E. Scuseria, *J. Chem. Phys.*, 2006, **125**, 224106.
85 L. Schimka, J. Harl and G. Kresse, *J. Chem. Phys.*, 2011, **134**, 024116.
86 T. M. Henderson, A. F. Izmaylov, G. E. Scuseria and A. Savin, *J. Chem. Phys.*, 2007, **127**, 221103.
87 T. M. Henderson, A. F. Izmaylov, G. E. Scuseria and A. Savin, *J. Chem. Theory Comput.*, 2008, **4**, 1254–1262.
88 J. F. Liu, S. Yin, H. P. Wu, Y. W. Zeng, X. R. Hu, Y. W. Wang, G. L. Lv and J. Z. Jiang, *J. Phys. Chem. B*, 2006, **110**, 21588–21592.
89 H. Sawada, *Mater. Res. Bull.*, 1994, **29**, 239–245.
90 S. Asbrink and A. Waskowska, *J. Condens. Matter Phys.*, 1991, **3**, 8173–8180.
91 N. Pailhé, A. Wattiaux, M. Gaudon and A. Demourgues, *J. Solid State Chem.*, 2008, **181**, 2697–2704.
92 S. Sasaki, K. Fujino and Y. Takéuchi, *Proc. Jpn. Acad., Ser. B*, 1979, **55**, 43–48.
93 W. R. Robinson, *Acta Crystallogr., Sect. B: Struct. Crystallogr. Cryst. Chem.*, 1975, **31**, 1153–1160.
94 A. Kirfel and K. Eichhorn, *Acta Crystallogr., Sect. A: Found. Crystallogr.*, 1990, **46**, 271–284.
95 S. C. Abrahams and J. L. Bernstein, *J. Chem. Phys.*, 1971, **55**, 3206–3211.
96 V. Shklover, T. Haibach, F. Ried, R. Nesper and P. Novák, *J. Solid State Chem.*, 1996, **123**, 317–323.
97 I. A. Kaurova, G. M. Kuz'micheva and V. B. Rybakov, *Crystallogr. Rep.*, 2013, **58**, 226–233.
98 C. Rödl, F. Sottile and L. Reining, *Phys. Rev. B: Condens. Matter Mater. Phys.*, 2015, **91**(4), 045102.
99 B. N. Brockhouse, *J. Chem. Phys.*, 1953, **21**, 961–962.
100 L. Patrick, *Phys. Rev.*, 1954, **93**, 370.
101 M. S. Kuklin and A. J. Karttunen, *J. Phys. Chem. C*, 2018, **122**, 24949–24957.
102 S. Grimme, J. Antony, S. Ehrlich and H. Krieg, *J. Chem. Phys.*, 2010, **132**, 154104.
103 S. Grimme, S. Ehrlich and L. Goerigk, *J. Comput. Chem.*, 2011, **32**, 1456–1465.
104 A. O. de-la Roza, L. M. LeBlanc and E. R. Johnson, *Phys. Chem. Chem. Phys.*, 2020, **22**, 8266–8276.
105 W. Ouyang, I. Azuri, D. Mandelli, A. Tkatchenko, L. Kronik, M. Urbakh and O. Hod, *J. Chem. Theory Comput.*, 2019, **16**, 666–676.
106 A. M. Reilly and A. Tkatchenko, *J. Chem. Phys.*, 2013, **139**, 024705.
107 M. Ferrero, M. Rérat, B. Kirtman and R. Dovesi, *J. Chem. Phys.*, 2008, **129**, 244110.
108 M. Ferrero, M. Rérat, R. Orlando and R. Dovesi, *J. Comput. Chem.*, 2008, **29**, 1450–1459.
109 M. Ferrero, M. Rérat, R. Orlando and R. Dovesi, *J. Chem. Phys.*, 2008, **128**, 014110.
110 W. Setyawan and S. Curtarolo, *Comput. Mater. Sci.*, 2010, **49**, 299–312.
111 J. Paier, M. Marsman and G. Kresse, *J. Chem. Phys.*, 2007, **127**, 024103.
112 N. Marom, A. Tkatchenko, M. Rossi, V. V. Gobre, O. Hod, M. Scheffler and L. Kronik, *J. Chem. Theory Comput.*, 2011, **7**, 3944–3951.

113 J. Kanamori, *J. Phys. Chem. Solids*, 1959, **10**, 87–98.
114 C. M. Zicovich-Wilson, F. Pascale, C. Roetti, V. R. Saunders, R. Orlando and R. Dovesi, *J. Comput. Chem.*, 2004, **25**, 1873–1881.
115 F. Pascale, C. M. Zicovich-Wilson, F. L. Gejo, B. Civalleri, R. Orlando and R. Dovesi, *J. Comput. Chem.*, 2004, **25**, 888–897.
116 L. Maschio, B. Kirtman, M. Rérat, R. Orlando and R. Dovesi, *J. Chem. Phys.*, 2013, **139**, 164101.
117 L. Maschio, B. Kirtman, S. Salustro, C. M. Zicovich-Wilson, R. Orlando and R. Dovesi, *J. Phys. Chem. A*, 2013, **117**, 11464–11471.
118 H. Ding and B. Xu, *J. Chem. Phys.*, 2012, **137**, 224509.
119 C. Yang and C. Wöll, *Adv. Phys.: X*, 2017, **2**, 373–408.
120 J. L. Lansford, A. V. Mironenko and D. G. Vlachos, *Nat. Commun.*, 2017, **8**(1842), 1–9.
121 B. Hammer, L. B. Hansen and J. K. Nørskov, *Phys. Rev. B: Condens. Matter Mater. Phys.*, 1999, **59**, 7413–7421.
122 P. M. Sarte, M. Songvilay, E. Pachoud, R. A. Ewings, C. D. Frost, D. Prabhakaran, K. H. Hong, A. J. Browne, Z. Yamani, J. P. Attfield, E. E. Rodriguez, S. D. Wilson and C. Stock, *Phys. Rev. B*, 2019, **100**(7), 075143.
123 F. Parmigiani and L. Sangaletti, *J. Electron Spectrosc. Relat. Phenom.*, 1999, **98–99**, 287–302.
124 H. Chou and H. Y. Fan, *Phys. Rev. B: Condens. Matter Mater. Phys.*, 1974, **10**, 901–910.
125 E. Z. Kurmaev, R. G. Wilks, A. Moewes, L. D. Finkelstein, S. N. Shamin and J. Kuneš, *Phys. Rev. B: Condens. Matter Mater. Phys.*, 2008, **77**(16), 165127.
126 M. Heinemann, B. Eifert and C. Heiliger, *Phys. Rev. B: Condens. Matter Mater. Phys.*, 2013, **87**(11), 115111.
127 F. Marabelli, G. B. Parravicini and F. Salghetti-Drioli, *Phys. Rev. B: Condens. Matter Mater. Phys.*, 1995, **52**, 1433–1436.
128 P. W. Baumeister, *Phys. Rev.*, 1961, **121**, 359–362.
129 L. Marusak, R. Messier and W. B. White, *J. Phys. Chem. Solids*, 1980, **41**, 981–984.
130 H. Yamada, X.-G. Zheng, Y. Soejima and M. Kawaminami, *Phys. Rev. B: Condens. Matter Mater. Phys.*, 2004, **69**(10), 104104.
131 D.-H. Seo, A. Urban and G. Ceder, *Phys. Rev. B: Condens. Matter Mater. Phys.*, 2015, **92**(11), 115118.
132 R. G. Compton, *Understanding voltammetry*, World Scientific, New Jersey, London, 2018.
133 J. B. Goodenough, *Phys. Rev.*, 1968, **171**, 466–479.
134 K. Yim, Y. Youn, M. Lee, D. Yoo, J. Lee, S. H. Cho and S. Han, *Npj Comput. Mater.*, 2018, **4**(17), 1–7.
135 J. O. Sofo and G. D. Mahan, *Phys. Rev. B: Condens. Matter Mater. Phys.*, 1994, **49**, 4565–4570.
136 A. Getsoian, Z. Zhai and A. T. Bell, *J. Am. Chem. Soc.*, 2014, **136**, 13684–13697.
137 Y. Kang, Y. Youn, S. Han, J. Park and C.-S. Oh, *Chem. Mater.*, 2019, **31**, 4072–4080.
138 J. K. Nørskov, F. Abild-Pedersen, F. Studt and T. Bligaard, *Proc. Natl. Acad. Sci. U. S. A.*, 2011, **108**, 937–943.
139 B. Hammer and J. Nørskov, *Surf. Sci.*, 1995, **343**, 211–220.
140 B. Hammer and J. Nørskov, *Advanced Catalysis*, Elsevier, 2000, pp. 71–129.
141 B. Civalleri, D. Presti, R. Dovesi and A. Savin, *Chemical Modelling: Applications and Theory*, The Royal Society of Chemistry, 2012, vol. 9, pp. 168–185.
142 J. P. Perdew, *Int. J. Quantum Chem.*, 2009, **28**, 497–523.
143 P. García-Fernández, J. C. Wojdeł, J. Íñiguez and J. Junquera, *Phys. Rev. B*, 2016, **93**(19), 195137.
144 E. J. Baerends, *Phys. Chem. Chem. Phys.*, 2017, **19**, 15639–15656.
145 H. Xiao, J. Tahir-Kheli and W. A. Goddard, *J. Phys. Chem. Lett.*, 2011, **2**, 212–217.
146 J. M. Crowley, J. Tahir-Kheli and W. A. Goddard, *J. Phys. Chem. Lett.*, 2016, **7**, 1198–1203.
147 Y. Zhang, J. Furness, R. Zhang, Z. Wang, A. Zunger and J. Sun, *Phys. Rev. B*, 2020, **102**(4), 045112.
148 G. Trimarchi, Z. Wang and A. Zunger, *Phys. Rev. B*, 2018, **97**(3), 035107.
149 J. P. Perdew, A. Ruzsinszky, J. Sun, N. K. Nepal and A. D. Kaplan, *Proc. Natl. Acad. Sci. U. S. A.*, 2021, **118**, e2017850118.
150 R. S. Mulliken, *J. Chem. Phys.*, 1955, **23**, 1833–1840.
151 K. A. Moltved and K. P. Kepp, *J. Phys. Chem. C*, 2019, **123**, 18432–18444.
152 K. B. Wiberg and P. R. Rablen, *J. Org. Chem.*, 2018, **83**, 15463–15469.
153 M. D. Towler, N. L. Allan, N. M. Harrison, V. R. Saunders, W. C. Mackrodt and E. Aprà, *Phys. Rev. B: Condens. Matter Mater. Phys.*, 1994, **50**, 5041–5054.
154 P. Geerlings, F. D. Proft and W. Langenaeker, *Chem. Rev.*, 2003, **103**, 1793–1874.
155 N. Glebko, I. Aleksandrova, G. C. Tewari, T. S. Tripathi, M. Karppinen and A. J. Karttunen, *J. Phys. Chem. C*, 2018, **122**, 26835–26844.
156 C. Ertural, S. Steinberg and R. Dronskowski, *RSC Adv.*, 2019, **9**, 29821–29830.
157 S. Saha, R. K. Roy and P. W. Ayers, *Int. J. Quantum Chem.*, 2008, **109**, 1790–1806.
158 C. Andreasen, T. Hao, J. Hatoum and Z. M. Hossain, *J. Appl. Phys.*, 2021, **130**, 034303.
159 J. L. Mancuso, A. M. Mroz, K. N. Le and C. H. Hendon, *Chem. Rev.*, 2020, **120**, 8641–8715.
160 T. Bredow and A. R. Gerson, *Phys. Rev. B: Condens. Matter Mater. Phys.*, 2000, **61**, 5194–5201.
161 A. J. Merer, *Annu. Rev. Phys. Chem.*, 1989, **40**, 407–438.
162 R. Radwanski and Z. Ropka, *Phys. B*, 2004, **345**, 107–110.
163 A. Schrön, C. Rödl and F. Bechstedt, *Phys. Rev. B: Condens. Matter Mater. Phys.*, 2012, **86**(11), 115134.
164 A. K. Cheetham and D. A.-O. Hope, *Phys. Rev. B: Condens. Matter Mater. Phys.*, 1983, **27**, 6964–6967.
165 X. Xu and D. G. Truhlar, *J. Chem. Theory Comput.*, 2011, **8**, 80–90.
166 S. K. Kwon and B. I. Min, *Phys. Rev. B: Condens. Matter Mater. Phys.*, 2000, **62**, 73–75.
167 P. Pyykkö, *Annu. Rev. Phys. Chem.*, 2012, **63**, 45–64.
168 A. M. Olés, *J. Phys., Colloq.*, 1988, **49**, C8-43–C8-48.
169 M. Pouchard, A. Villesuzanne and J.-P. Doumerc, *C. R. Chim*, 2003, **6**, 135–145.

170 J. Shee, M. Loipersberger, D. Hait, J. Lee and M. Head-Gordon, *J. Chem. Phys.*, 2021, **154**, 194109.
171 K. S. Kumar, G. L. Prajapati, R. Dagar, M. Vagadia, D. S. Rana and M. Tonouchi, *Adv. Optical Mater.*, 2019, **8**, 1900958.
172 J. Ngai, F. Walker and C. Ahn, *Annu. Rev. Mater. Res.*, 2014, **44**, 1–17.
173 A. Szabo and N. S. Ostlund, *Modern quantum chemistry*, Dover Publications, Mineola, NY, 1996.
174 A. J. Cohen, D. J. Tozer and N. C. Handy, *J. Chem. Phys.*, 2007, **126**, 214104.
175 J. Wang, A. D. Becke and V. H. Smith, *J. Chem. Phys.*, 1995, **102**, 3477–3480.
176 J. M. Wittbrodt and H. B. Schlegel, *J. Chem. Phys.*, 1996, **105**, 6574–6577.
177 D. Casanova and A. I. Krylov, *Phys. Chem. Chem. Phys.*, 2020, **22**, 4326–4342.
178 A. S. Menon and L. Radom, *J. Phys. Chem. A*, 2008, **112**, 13225–13230.
179 C. J. Schattenberg, T. M. Maier and M. Kaupp, *J. Chem. Theory Comput.*, 2018, **14**, 5653–5672.
180 K. Tada, S. Yamanaka, T. Kawakami, Y. Kitagawa, M. Okumura, K. Yamaguchi and S. Tanaka, *Chem. Phys. Lett.*, 2021, **765**, 138291.
181 B. Bleaney and B. Bleaney, *Electromagnetic Theory*, 1976.
182 H. Pan, A. Kursumovic, Y.-H. Lin, C.-W. Nan and J. L. MacManus-Driscoll, *Nanoscale*, 2020, **12**, 19582–19591.
183 C. T. Chen, J. Pedrini, E. A. Gaulding, C. Kastl, G. Calafiore, S. Dhuey, T. R. Kuykendall, S. Cabrini, F. M. Toma, S. Aloni and A. M. Schwartzberg, *Sci. Rep.*, 2019, **9**(2768), 1–9.
184 K. Yim, Y. Yong, J. Lee, K. Lee, H.-H. Nahm, J. Yoo, C. Lee, C. S. Hwang and S. Han, *NPG Asia Mater.*, 2015, **7**, e190.
185 J. Zhang, J. Shi, D.-C. Qi, L. Chen and K. H.-L. Zhang, *APL Mater.*, 2020, **8**, 020906.